ELSEVIER

Contents lists available at ScienceDirect

Chemical Geology

journal homepage: www.elsevier.com/locate/chemgeo





Evaluating reference materials and common-Pb corrections for high-resolution apatite U—Pb geochronology

Francisco E. Apen^{a,*}, Sean P. Gaynor^a, Blair Schoene^a, John M. Cottle^b

- a Department of Geosciences, Princeton University, Princeton, NJ, USA
- ^b Department of Earth Science, University of California, Santa Barbara, CA, USA

ARTICLE INFO

Editor: Marco Fiorentini

Keywords:
Apatite
U-Pb
Geochronology
Thermochronology
ID-TIMS
LA-ICP-MS

ABSTRACT

We report isotope dilution thermal ionization mass spectrometry (ID-TIMS) and laser ablation split stream inductively coupled plasma mass spectrometry (LASS) U-Pb data for a suite of widely available reference apatites: Fish Canyon Tuff, Mount Dromedary, TEMORA 2, and Duluth Complex anorthosite. We apply different common-Pb correction strategies to the U—Pb data sets; (1) anchoring to a Stacey and Kramers (1975) model Pb composition; (2) unanchored 2-D ²³⁸U/²⁰⁶Pb-²⁰⁷Pb/²⁰⁶Pb isochron regressions; and (3) unanchored 3-D $^{238}\text{U}/^{206}\text{Pb}-^{207}\text{Pb}/^{206}\text{Pb}-^{204}\text{Pb}/^{206}\text{Pb}$ isochron regressions. The different common-Pb corrections yield consisting the contract of the contr tent dates within each ID-TIMS and LASS data set, with 3-D regression method producing the highest precision isochrons. FCT apatite produces an ID-TIMS 3-D isochron age of 28.8 \pm 3.7 Ma with (207 Pb) $_i$ = 0.851 \pm 0.021. Mount Dromedary apatite yields an ID-TIMS 3-D isochron age of 98.4 \pm 0.5 Ma with (207 Pb) i = 0.839 ± 0.003 . TEMORA 2 apatite has an ID-TIMS 3-D isochron age of 402 ± 7 Ma and $(^{207}\text{Pb}/^{206}\text{Pb})_i = 0.839$ \pm 0.008. Duluth Complex anorthosite apatite yields an ID-TIMS 3-D isochron age of 1077 \pm 9 Ma with $(^{207}\text{Pb}/^{206}\text{Pb})_i = 0.849 \pm 0.046$. The MSWDs associated with isochrons calculated from both the ID-TIMS and LASS data sets are larger than expected for a single age population, revealing complexities that are otherwise not captured by 2-D isochron methods. In the case of FCT apatite, the ID-TIMS data indicate significant heterogeneity in the initial Pb ratio ($(^{207}\text{Pb}/^{206}\text{Pb})_i = 0.845-0.856$), invalidating this sample as a viable reference apatite for high-precision geochronology. Additionally, the common-Pb compositions of TEMORA 2 and Duluth Complex anorthosite apatites calculated using the ID-TIMS data deviate from bulk Earth Pb evolution models beyond 2σ uncertainty. The data emphasize the utility of unanchored age regressions in generating the highest fidelity apatite U-Pb dates. Further, TEMORA 2 and Duluth Complex apatite ages are both younger than their corresponding zircon U-Pb ages, highlighting the need to independently verify the ages of prospective reference apatites.

1. Introduction

The phosphate mineral apatite $(Ca_5(PO_4)_3(OH,Cl,F))$ is a valuable chronometer and geochemical tracer of petrogenesis due to its ubiquity in various rock types and its ability to incorporate significant incompatible elements, including rare earth elements (REEs), Th, and U (e.g., Bea and Montero, 1999; Sha and Chappell, 1999; O'Reilly and Griffin, 2000; Belousova et al., 2002; Bruand et al., 2017; Henrichs et al., 2018, 2019; O'Sullivan et al., 2020). Experimental data indicate that thermally-mediated volume diffusion of U in apatite is negligible under all but the most extreme crustal temperatures (i.e., at >900 °C; Cherniak, 2005), whereas Pb is diffusively mobile at temperatures above

350–550 °C (Cherniak et al., 1991; Chew et al., 2014; Smye et al., 2018). This suggests that apatite acts as a U—Pb thermochronometer, and indeed, many studies have exploited the U—Pb systematics of apatite to reconstruct thermal histories of magmatic and orogenic systems (e.g., Krogstad and Walker, 1994; Chamberlain and Bowring, 2001; Schmitz and Bowring, 2003; Schoene and Bowring, 2007; Chew et al., 2011; Thomson et al., 2012; Cochrane et al., 2014; Seymour et al., 2016; Ibanez-Mejia et al., 2018; Paul et al., 2019). However, it is apparent that apatite does not always simply behave as a thermochronometer, but is subject to neo/recrystallization during metamorphism, fluid-rock interactions, and deformation, as indicated by correlations among U—Pb dates, trace element compositions, and microtextures (e.g., Corfu and

E-mail address: feapen@princeton.edu (F.E. Apen).

 $^{^{\}ast}$ Corresponding author.

Stone, 1998; Schoene and Bowring, 2007; Zirner et al., 2015; Gawęda et al., 2018; Kirkland et al., 2017, 2018; Henrichs et al., 2019; Glorie et al., 2019; Prent et al., 2020; Ribeiro et al., 2020; Apen et al., 2020; Odlum et al., 2022; Dusséaux et al., 2022). Apatite can therefore be used to directly constrain the timing and duration of fluid flow and deformation in rocks.

Despite the proliferation of apatite U—Pb dating as a tool to investigate myriad processes, reconstructing high-resolution geological histories using apatite is not always straightforward. One significant challenge arises from apatite's propensity to incorporate significant amounts of non-radiogenic (common) Pb during crystallization, requiring corrections to obtain accurate and geologically meaningful U—Pb dates. Ways to correct for common-Pb include: (1) implementing an initial common-Pb composition ((²⁰⁷Pb/²⁰⁶Pb)_i) from a bulk Earth Pb growth model (e.g., Stacey and Kramers, 1975; Chew et al., 2011); (2) utilizing the Pb isotopic composition of cogenetic, low U/Pb phases (e. g., Krogstad and Walker, 1994; Chamberlain and Bowring. 2001: Schoene and Bowring, 2006; Schoene and Bowring, 2007; Ibanez-Mejia et al., 2018); (3) unanchored linear regressions through multiple U—Pb data points that form a 2-D ²³⁸U/²⁰⁶Pb-²⁰⁷Pb/²⁰⁶Pb isochron (e.g., Ludwig, 1998; Schoene and Bowring, 2006; Chew et al., 2011; Chew et al., 2014); and (4) unanchored regressions to yield a 3-D 238 U/ 206 Pb- 207 Pb/ 206 Pb- 204 Pb/ 206 Pb isochron (the total Pb—U method; Ludwig, 1998; Storey et al., 2006; Schoene and Bowring, 2006; Chew et al., 2011; Chew et al., 2014; Paul et al., 2021; Apen et al., 2022).

Each approach listed above has advantages and limitations. Assuming a (207Pb/206Pb)_i composition based on the two-stage Pb evolution model of Stacey and Kramers (1975) is straightforward but this approach is not always appropriate for apatite as it may crystallize from a Pb reservoir (or reservoirs) compositionally distinct from bulk Earth Pb models, such that the use of a model Pb composition will yield inaccurate dates (e.g., Bea and Montero, 1999; Schoene and Bowring, 2006; Paul et al., 2021). Utilizing the Pb isotopic composition of a low U/Pb mineral phase(s) is predicated on the assumption that they are cogenetic with apatite, which can be difficult to assess in the case of detrital or polymetamorphic rocks (e.g., Chew et al., 2011; Thomson et al., 2012; Kirkland et al., 2018). Even in rocks with relatively simple thermal histories (e.g., cooling of a magmatic body), the common-Pb composition of apatite is not always consistent with the common-Pb compositions of low U/Pb minerals (e.g., alkali feldspar; Chamberlain and Bowring, 2001; Schoene and Bowring, 2006). Analyses of multiple coeval apatites can define a ²³⁸U/²⁰⁶Pb-²⁰⁷Pb/²⁰⁶Pb isochron that enable age determinations without a priori assumptions of common-Pb composition. Considering ²⁰⁴Pb/²⁰⁶Pb as a third axis, the total Pb—U isochron method can similarly be used to calculate a U-Pb date and common-Pb intercept (Ludwig, 1998). Although the total Pb-U method arguably produces the most robust dates (e.g., Schoene and Bowring, 2006), 204Pb measurements have not routinely been considered in inductively coupled plasma mass spectrometry (ICP-MS) studies because ²⁰⁴Pb is the least abundant Pb isotope, and therefore the most challenging to measure accurately. An additional issue in obtaining robust ²⁰⁴Pb measurements with LA-ICP-MS stems from the isobaric interference of ²⁰⁴Hg present in the plasma and carrier gas, though the ²⁰⁴Hg interference can be removed if ²⁰²Hg is measured accurately (e.g., Horstwood et al., 2003; Chew et al., 2014). Another way forward is provided by collision cell ICP-MS, which enables removal of the ²⁰⁴Hg interference through the introduction of reaction gases in the ICP-MS (e. g., Gilbert and Glorie, 2020).

Generating the most precise and accurate apatite U—Pb dates, and by extension the highest fidelity geological histories, requires scrutinizing different common-Pb correction strategies and developing reference materials as analytical benchmarks. We provide isotope dilution thermal ionization mass spectrometry (ID-TIMS) U—Pb data for four widely available reference apatites—Fish Canyon tuff, Mount Dromedary, TEMORA 2, and Duluth Complex. The new ID-TIMS data for these apatites enables an assessment of different common-Pb corrections

methods for producing high-precision isochrons. The ID-TIMS data also provide a means to evaluate different common-Pb correction strategies for LA-ICP-MS data, with implications for the viability of the four apatites as reference materials for in situ U—Pb geo/thermochronology.

1.1. Samples and previous U—Pb geochronology

Aliquots of apatite were procured from GeoSep Services (http://geoseps.com/), from rocks with previously established high-precision U—Pb ID-TIMS zircon dates. These zircon dates, along with previously reported Ar—Ar dates and apatite U—Pb dates, where available, are summarized below and in Table 1. All quoted age uncertainties are 2σ , as reported in their respective sources, and are reported here as \pm X (Y) [Z], where X is the analytical uncertainty, Y includes analytical and U—Pb tracer calibration uncertainties, and Z includes analytical, U—Pb tracer calibration, and decay constant uncertainties (Jaffey et al., 1971).

Table 1Comparison of ages from Fish Canyon tuff (FCT), Mount Dromedary (MD), TEMORA 2 (TEM2), and Duluth anorthosite (AS).

Sample	Reported age and uncertainty (Ma) ¹	Method	References			
FCT	28.305 ± 0.036 28.201 ± 0.046	Ar-Ar sanidine	Renne et al. (2010)			
	[0.105]	Ar-Ar sanidine	Kuiper et al. (2008)			
	$28.172 \pm 0.028 [1.03]$ 28.478 ± 0.024	Ar-Ar sanidine	Rivera et al. (2011) Schmitz and Bowring			
	(0.058) [0.064]	U-Pb zircon ID-TIMS	(2001)			
		U-Pb zircon ID-TIMS	Bachmann et al.			
	$28.30 \pm 0.11 \; [0.159]$	(youngest)	(2007)			
	00 67 + 0 10 50 1007	U-Pb zircon ID-TIMS	Bachmann et al.			
	$28.67 \pm 0.13 \ [0.188]$	(oldest)	(2007)			
	28.196 ± 0.038 [0.058]	U-Pb zircon CA-ID- TIMS (youngest)	Wotzlaw et al. (2013)			
	28.638 ± 0.025	U-Pb zircon CA-ID-	Wotziaw et al. (2013)			
	[0.039]	TIMS (oldest)	Wotzlaw et al. (2013)			
	[]	Bayesian eruption				
	$28.18 \pm 0.04 \; [0.060]$	age	Keller et al. (2018)			
		U-Pb apatite LA-ICP-				
	26 ± 12	MS	Chew et al. (2014)			
			McDougall and			
MD	$97.9 \pm 1.8 \ [3.33]$	K-Ar biotite	Roksandic (1974)			
	$98.79 \pm 0.96 \; [2.18]$	K-Ar biotite	Renne et al. (1998) Spell and McDougall			
	$98.5 \pm 0.8 \; [1.97]$	K-Ar biotite	(2003)			
	$99.12 \pm 0.02 (0.03)$	U-Pb zircon CA-ID-				
FFF 40	[0.14]	TIMS	Schoene et al. (2006)			
TEM2	$416.78 \pm 0.33 \; [1.3]$	U-Pb zircon ID-TIMS U-Pb zircon CA-ID-	Black et al. (2004)			
	$418.37 \pm 0.14 \; [0.20]$	TIMS	Mattinson (2010)			
	$417.353 \pm 0.052 \\ [0.077]$	U-Pb zircon CA-ID- TIMS	Schaltegger et al. (2021)			
			Paces and Miller			
AS	1099.1 ± 0.5	U-Pb zircon ID-TIMS	(1993)			
	$1099.1 \pm 0.2 [1.2]$	U-Pb zircon ID-TIMS	Schmitz et al. (2003)			
	$1095.9 \pm 0.2 (0.3)$	U-Pb zircon CA-ID- TIMS	Cohoono et el (2006)			
	[1.4]	U-Pb zircon CA-ID-	Schoene et al. (2006)			
	$1095.32 \pm 0.33 [0.47]$	TIMS	Mattinson (2010)			
	10,0102 ± 0100 [0117]	U-Pb zircon CA-ID-	Ibañez-Mejia and			
	$1095.97 \pm 0.22 \hspace{1mm} [0.31]$	TIMS	Tissot (2019)			
	$1095.69 \pm 0.18 (0.35)$	U-Pb zircon CA-ID-	Swanson-Hysell et al.			
	[1.14]	TIMS	(2021)			
	$1095.81 \pm 0.16 (0.34)$	U-Pb zircon CA-ID-	Swanson-Hysell et al.			
	[1.14]	TIMS	(2021)			
	1070 47	U-Pb apatite LA-ICP-	Thomson et al.			
	1079 ± 47	MS U-Pb apatite LA-ICP-	(2012)			
	1078 ± 12	MS	Härtel et al. (2023)			

 $^{^1}$ All quoted age uncertainties are 2σ , as reported in their respective sources. Reported here as \pm X (Y) [Z], where X is the analytical uncertainty, Y includes analytical and U—Pb tracer calibration uncertainties, and Z includes analytical, U—Pb tracer calibration, and decay constant uncertainties (Jaffey et al., 1971).

1.1.1. Fish Canyon tuff

The Fish Canyon tuff (FCT) is a $\sim 5000 \text{ km}^3$ ignimbrite that erupted from the Oligocene La Garita caldera, part of the San Juan volcanic field in southwest Colorado, USA (e.g., Bachmann and Bergantz, 2003; Wotzlaw et al., 2013). Minerals from the FCT were originally targeted as reference materials (RMs) because the unit cooled rapidly upon eruption, is not tectonically overprinted, and is easily accessible for sampling. As such, there are various geochronological data sets for the FCT, including Ar-Ar and U-Pb geochronology (e.g., Lanphere and Baadsgaard, 2001; Renne et al., 2010; Rivera et al., 2011; Wotzlaw et al., 2013). Fish Canyon sanidine serves as a common neutron fluence monitor for ⁴⁰Ar—³⁹Ar geochronology. Renne et al. (2010) reported a $^{40}\text{Ar}\text{--}^{39}\text{Ar}$ age of 28.305 \pm 0.036 Ma for FCT sanidine based on intercalibrated ⁴⁰Ar—³⁹Ar and ²³⁸U/²⁰⁶Pb dates from rocks displaying closed-system behavior for both isotopic systems (later revised to 28.294 \pm 0.036 Ma in Renne et al., 2011). An 40 Ar $^{-39}$ Ar age of 28.201 \pm 0.046 [1.05] Ma for FCT sanidine is based on intercalibrated ⁴⁰Ar—³⁹Ar and astronomically tuned ages from marine deposits in Morocco (Kuiper et al., 2008). A similar calibration using an astronomically tuned section in Crete yielded an indistinguishable 40 Ar $^{-39}$ Ar age of 28.172 \pm 0.028 [1.03] Ma for FCT sanidine (Rivera et al., 2011).

Zircon U—Pb geochronology of the FCT indicates a protracted preeruptive magmatic history. Schmitz and Bowring (2001) dated FCT zircon using ID-TIMS utilizing an air-abrasion pretreatment and obtained a 230 Th-corrected weighted mean 206 Pb/ 238 U date of 28.478 \pm 0.024 (0.058) [0.064] Ma (MSWD = 0.97; n = 30); of the 30 analyses, 23were single crystals and seven were multi-grain fractions. Bachmann et al. (2007) presented air-abrasion ID-TIMS U—Pb zircon dates for eight single crystals and three multi-grain fractions, which yielded ²³⁰Thcorrected $^{206}\text{Pb}/^{238}\text{U}$ dates between 28.67 \pm 0.13 [0.188] Ma and 28.30 \pm 0.11 [0.159] Ma. Wotzlaw et al. (2013) presented single crystal U—Pb dates for 24 FCT zircons, prepared using chemical abrasion (CA) ID-TIMS (Mattinson, 2005), which yielded ²³⁰Th-corrected ²⁰⁶Pb/²³⁸U dates that range from 28.638 \pm 0.025 [0.039] Ma to 28.196 \pm 0.038 [0.058] Ma. Recently, Keller et al. (2018) applied a Bayesian eruption age model to the U-Pb zircon data from Wotzlaw et al. (2013) and suggested an eruption age of 28.18 \pm 0.04 [0.060] Ma (2 σ) for the FCT. Chew et al. (2014) reported a 26 \pm 12 Ma 238 U/ 206 Pb- 207 Pb/ 206 Pb isochron with a $(^{207}\text{Pb}/^{206}\text{Pb})_i$ intercept = 0.85 ± 0.02 (MSWD = 2.3; n= 17) for FCT apatite, obtained using LA-ICP-MS.

1.1.2. Mount dromedary

The Mount Dromedary (MD) apatite comes from a monzonite that is part of the Late Cretaceous Mount Dromedary intrusive complex in New South Wales, Australia (Boesen and Joplin, 1972). Mount Dromedary biotite (referred to as GA-1550 in the Ar—Ar literature) has been employed as a primary K—Ar RM due to its remarkable homogeneity. Multiple studies have reported consistent K—Ar dates: 97.9 ± 1.8 [3.33] Ma (McDougall and Roksandic, 1974), 98.79 ± 0.96 [2.18] Ma (Renne et al., 1998), and 98.5 ± 0.8 [1.97] Ma (Spell and McDougall, 2003). Schoene et al. (2006) dated zircon from this unit (sample RSES01–98) using CA-ID-TIMS and obtained a weighted mean $^{206}\text{Pb}/^{238}\text{U}$ date of 99.12 ± 0.02 (0.03) [0.14] Ma (MSWD = 1.0; n=10).

1.1.3. TEMORA 2

TEMORA 2 (referred to as TEM2 in this study) is from the Middledale gabbroic diorite from the Paleozoic Lachlan Orogen, eastern Australia (e.g., Black et al., 2004, and references therein). TEMORA 2 zircon dated using ID-TIMS by Black et al. (2004) using either physical abrasion or no pretreatment and produced a weighted mean $^{206}\text{Pb}/^{238}\text{U}$ date of 416.78 \pm 0.33 [1.3] Ma (MSWD = 0.56; n = 9). Mattinson (2010) dated TEM2 zircon using multi-step partial dissolution CA-ID-TIMS and calculated a weighted mean CA-ID-TIMS $^{206}\text{Pb}/^{238}\text{U}$ date of 418.37 \pm 0.14 [0.20] Ma (MSWD = 0.98; n = 11). Schaltegger et al. (2021) calculated a weighted mean CA-ID-TIMS $^{206}\text{Pb}/^{238}\text{U}$ date of 417.353 \pm 0.052 [0.077] Ma (MSWD = 4.4; n = 59).

1.1.4. Duluth complex anorthosite

Apatite AS comes from a gabbroic anorthosite that is part of the Duluth Complex, northern Minnesota, USA (e.g., Paces and Miller, 1993; Swanson-Hysell et al., 2021). The specific outcrop from which apatite in this study was extracted comes from Forest Center, commonly referred to as FC-1, but referred to AS henceforth to avoid confusion with FCT apatite. Various TIMS studies have generated high-precision U-Pb dates for zircon from Duluth Complex anorthosites, although not all analyses are of samples from the same outcrop. Paces and Miller (1993) presented a weighted mean ID-TIMS $^{207}\text{Pb}/^{206}\text{Pb}$ date of 1099.1 ± 0.5 Ma (MSWD = 0.38; n = 8) for a sample near Duluth (sample AS3) and 1099.0 ± 0.6 Ma (MSWD = 0.17; n = 6) for a sample near Forest Center (sample FC-1). Schmitz et al. (2003) produced an ID-TMS weighted mean $^{206}\text{Pb}/^{238}\text{U}$ date of 1099.1 \pm 0.2 [1.2] Ma (MSWD = 0.14; n = 12) for sample AS3. Schoene et al. (2006) dated zircon using CA-ID-TIMS and obtained a weighted mean $^{206}\text{Pb}/^{238}\text{U}$ date of 1095.9 \pm 0.2 (0.3) [1.4] Ma (MSWD = 0.5; n = 8) for sample AS3. Using multi-step partial dissolution CA-ID-TIMS, Mattinson (2010) calculated a weighted mean CA-ID-TIMS $^{206}\text{Pb}/^{238}\text{U}$ date of 1095.32 \pm 0.33 [0.47] Ma for sample FC-1 (MSWD = 1.0; n = 13). Ibañez-Mejia and Tissot (2019) obtained a weighted mean $^{206}\text{Pb}/^{238}\text{U}$ age of 1095.97 \pm 0.22 [0.31] Ma (MSWD = 0.54; n = 6) using CA-ID-TIMS for sample FC-1. Swanson-Hysell et al. (2021) obtained CA-ID-TIMS weighted mean $^{206}\text{Pb}/^{238}\text{U}$ date of $1095.81 \pm 0.16~(0.34)~[1.14]~{
m Ma}~({
m MSWD}=1.4;~n=10)~{
m and}~1095.69 \pm$ 0.18 (0.35) [1.14] (MSWD = 0.34; n = 7) for two different samples from the anorthosite series. McKanna et al. (2024) also report CA-ID-TIMS dates for AS3 zircon using different chemical abrasion conditions; they report weighted mean weighted mean $^{206}\text{Pb}/^{238}\text{U}$ dates of 1096.42 \pm $0.49\,\text{Ma}$ (MSWD $= 1.7;\, n = 6$) and $1096.29 \pm 0.36\,\text{Ma}$ (MSWD $= 2.3;\, n$ = 13) for zircon crystals treated at 210 °C and 180 °C, respectively. Thomson et al. (2012) reported a Wetherill concordia date of 1079 \pm 47 Ma (MSWD = 2.1; n = 10) for FC-1 apatite, measured using LA-ICP-MS. Recently, Härtel et al. (2023) reported a 1078 \pm 12 Ma ²³⁸U/²⁰⁶Pb-²⁰⁷Pb/²⁰⁶Pb isochron for FC-1 apatite (anchored with a Stacey and Kramers Pb_c), obtained using LA-ICP-MS.

2. Methods

2.1. ID-TIMS

Individual euhedral apatite crystals were handpicked under a binocular microscope in isopropyl alcohol and washed three times in distilled water to remove surface contamination. The cleaned apatite crystals were transferred into individual 200 μ L Savillex microcapsules. Concentrated HCl and a mixed $^{205}\text{Pb}-^{233}\text{U}-^{235}\text{U}$ tracer (ET535; Condon et al., 2015; McLean et al., 2015) were added to the microcapsules and the crystals were left to dissolve at 210 °C overnight in a Parr bomb. After dissolution, drying to salts on a hotplate, and redissolution in 1 M HBr, Pb and U were chemically purified from the dissolved material using dilute HBr- and HCl-based anion exchange chromatography (Krogh, 1973). The Pb and U aliquots were dried down separately with trace H₃PO₄ and loaded onto outgassed zone-refined Re ribbon filaments with a Si-gel emitter (Gerstenberger and Haase, 1997).

The U and Pb isotopes were measured on an IsotopX Phoenix TIMS at Princeton University. Lead isotopes were measured in dynamic mode using a Daly photomultiplier, and U isotopes were measured as an oxide in static mode using Faraday collectors coupled to $10^{12}~\Omega$ resistor amplifiers. Mass fractionation of Pb was calculated from previous repeat measurements of samples spiked with an ET2535 tracer solution (Condon et al., 2015), which yielded a value of $\alpha = 0.182 \pm 0.041\%$ a.m.u. The $^{18}\text{O}/^{16}\text{O}$ oxygen isotope composition in uranium oxide was assumed to be 0.002051 ± 0.000020 (2σ) based on previous measurements of the U500 standard (Szymanowski and Schoene, 2020). The mass fractionation of U was corrected using the composition of the spike solution (Condon et al., 2015), and the abundance of U was calculated using a sample composition $^{238}\text{U}/^{235}\text{U}$ of 137.818 ± 0.045 (2σ ; Hiess et al.,

2012). All analyses were corrected for laboratory blanks, estimated to contribute 0.36 \pm 0.15 pg of Pb during the HBr- and HCl-based anion exchange chromatography used in this study based on repeat measurements of total procedural blanks performed during the period of this study (n = 15). This blank yielded a composition of 206 Pb/ 204 Pb = 19.15 $\pm~0.27,~^{207}\text{Pb}/^{204}\text{Pb} = 16.00 \pm 0.19~\text{and}~^{208}\text{Pb}/^{204}\text{Pb} = 39.02 \pm 1.80~\text{(n)}$ = 15; 1 standard deviation). The U—Pb data and uncertainties for each analysis were calculated using the algorithms of Schmitz and Schoene (2007) and plotted using the IsoplotR software package (Vermeesch, 2018), with isochron ages calculated using discordia model-1 (Ludwig, 2012). Earthtime ET100Ma standard solution analyzed during the period of these analyses yielded a $^{206}\text{Pb}/^{238}\text{U}$ date of 100.1633 \pm 0.0093 Ma (MSWD = 0.93; n = 17), within uncertainty of the recently reported inter-laboratory calibrated value of 100.173 \pm 0.003 Ma for this solution (Schaltegger et al., 2021). The complete ID-TIMS data set is presented in Supplementary Table 1.

2.2. Cathodoluminescence imaging

Prior to LASS-ICP-MS analysis, aliquots of each apatite sample were poured into 0.125-in.-diameter Teflon molds and cast in epoxy. Once hardened, these miniature mounts were placed in a larger 1-in.-diameter mold, cast in epoxy again, polished, carbon coated, and imaged using cathodoluminescence (CL). CL images were generated using a FEI Quanta 400f field-emission scanning electron microscope (SEM)

equipped with a KE Developments Centaurus CL detector, housed at the University of California, Santa Barbara (UCSB). Representative images are shown in Fig. 1.

2.3. LASS-ICP-MS

Simultaneous U—Pb and trace element analysis of apatite was done using LASS-ICP-MS at the University of California, Santa Barbara (UCSB), following methods presented in Kylander-Clark et al. (2013). The LASS system consists of a Photon Machines 193 nm excimer Analyte laser with a HelEx-2 ablation cell coupled to a Nu Instruments Plasma 3D multi-collector (MC) ICP-MS for U—Pb isotopes and an Agilent 7700S quadrupole (Q)-ICP-MS for trace element measurements. On the MC-ICP-MS, $^{202}{\rm Hg},~^{204}({\rm Pb}~+~{\rm Hg}),~^{206}{\rm Pb},~^{207}{\rm Pb},~^{208}{\rm Pb}$ were measured on Daly detectors and $^{238}{\rm U}$ and $^{232}{\rm Th}$ were measured on Faraday collectors. On the Q-ICP-MS, the following masses were measured: $^{28}{\rm Si},~^{31}{\rm P},~^{44}{\rm Ca},~^{55}{\rm Mn},~^{88}{\rm Sr},~^{89}{\rm Y},~^{90}{\rm Zr},~^{139}{\rm La},~^{140}{\rm Ce},~^{141}{\rm Pr},~^{146}{\rm Nd},~^{147}{\rm Sm},~^{153}{\rm Eu},~^{157}{\rm Gd},~^{159}{\rm Tb},~^{163}{\rm Dy},~^{165}{\rm Ho},~^{166}{\rm Er},~^{169}{\rm Tm},~^{172}{\rm Yb},~^{105}{\rm Lu}.~^{Laser},~^{MC-ICP-MS},~^{and}{\rm Q-ICP-MS}$ parameters are presented in Table 2.

Apatite was ablated using a 35- μ m-diameter laser spot operating at a 5 Hz repetition rate with a laser fluence of ~ 1 J/cm² and an ablation rate of 50–100 nm per laser pulse. Each ablation sequence consisted of two cleaning shots followed by 18 s of baseline measurement and 15 s of ablation. Raw U—Pb ratios were baseline subtracted and corrected for laser- and plasma-induced element fractionation and instrument drift

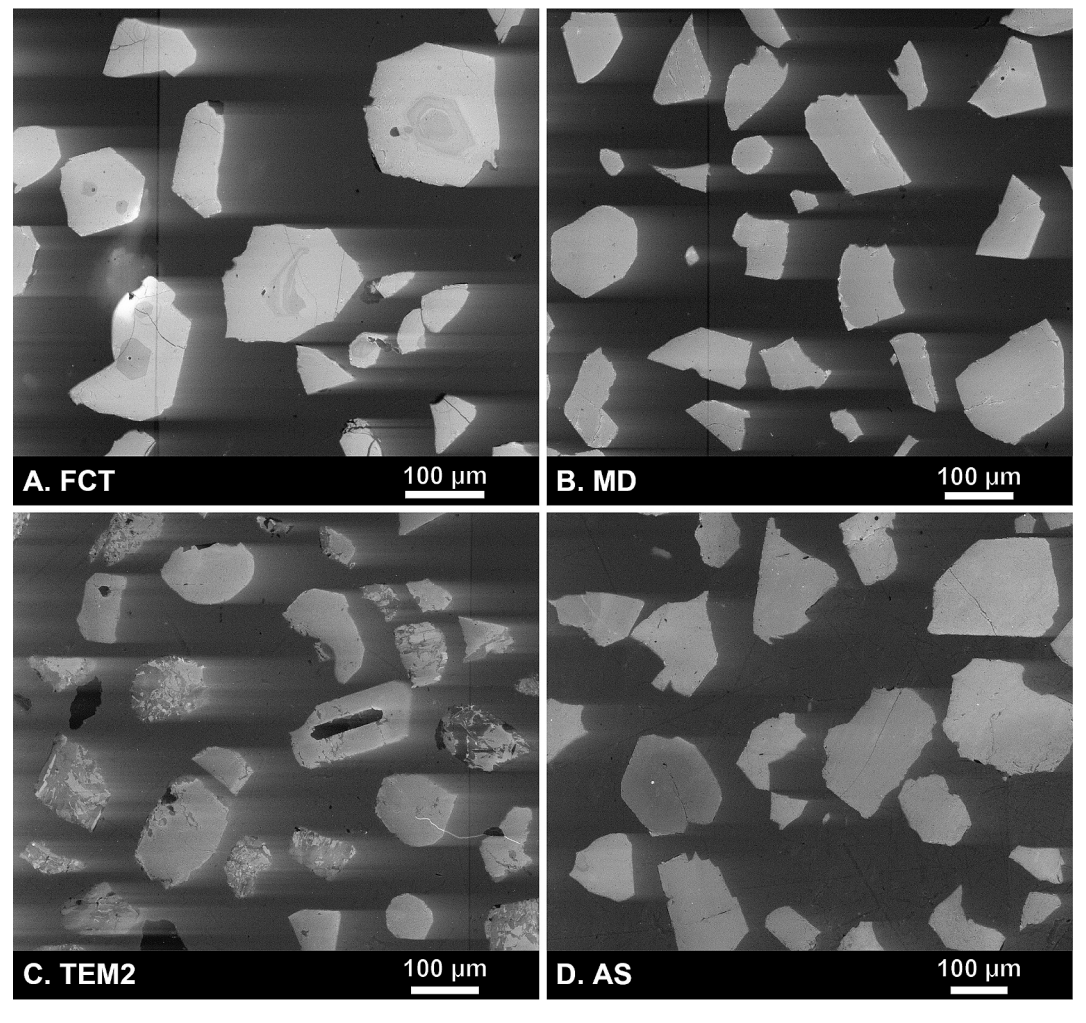


Fig. 1. Cathodoluminescence (CL) images of apatite samples. A) Fish Canyon apatite grains contain cores with concentric zoning. Notably, B) Mount Dromedary apatite is homogeneous. C) Some TEMORA 2 apatite grains show no distinctive internal features whereas others show complex, patchy CL bright and dark zones. CL dark domains in larger grains are quartz inclusions. D) Duluth anorthosite apatite shows faint oscillatory zonation but is otherwise featureless.

Table 2 ICP-MS and laser parameters used for U—Pb and TE LASS.

Instruments					
Instrument model	Nu Instruments Plasma 3D MC-ICP-MS	Agilent 7700S quadrupole			
RF power Make-up gas flow Masses measured	1300 W 1.76 L/min ²⁰² Hg, ²⁰⁴ Hg + Pb, ^{206,207,208} Pb on Dalys; ²³² Th, ²³⁸ U on Faraday cups	0.5 L/min ²⁸ Si, ³¹ P, ⁴⁴ Ca, ⁵⁵ Mn, ⁸⁸ Sr, ⁸⁹ Y, ⁹⁰ Zr, ¹³⁹ La, ¹⁴⁰ Ce, ¹⁴¹ Pr ¹⁴⁶ Nd, ¹⁴⁷ Sm, ¹⁵³ Eu, ¹⁵⁷ Gd, ¹⁵⁹ Tb, ¹⁶³ Dy, ¹⁶⁵ Ho, ¹⁶⁶ Er, ¹⁶⁹ Tm, ¹⁷² Yb, ¹⁷⁵ Lu			
Integration time per peak/dwell times; quadrupole sweep time	100 ms	~200 ms			
Total integration (sweep) time per output data point	0.1 s	0.5 s			

Laser ablation system					
Make, Model and type	Cetac Teledyne 193 nm excimer Analyte laser				
Ablation cell and volume	HelEx-2 ablation cell (Eggins et al., 1998, 2005)				
Laser wavelength	193 nm				
Pulse width	4 ns				
Fluence; pit depth/pulse	~1 J/cm²; ~0.08–0.1 µm/pulse				
Repetition rate	5 Hz				
Ablation duration	15 s				
Spot diameter	35 μm				
Sampling mode / pattern	Static spot ablation				
Carrier gas	100% He in the cell, Ar make-up gas combined in				
	a glass mixing bulb				
Cell carrier gas flow	0.105 L/min total (0.08 L/min for cup, 0.025 L/				
	min for cell)				
Data Processing					
_	MAD-UCSB (Apen et al., 2022), MRC-1 (Apen				
Reference Materials	et al., 2022), BRZ-1 (Apen et al. (2022), McClure				
Reference Materials	Mountain (Schoene and Bowring, 2006), NIST-				
	612 (Pearce et al. (1997)				
	iolite v. 4 (Paton et al., 2010, 2011); LIEF				
Data processing package	612 (Pearce et al. (1997) iolite v. 4 (Paton et al., 2010, 2011); LIEF correction assumes reference material and				
	samples behave identically.				
Common-Pb correction,	No common-Pb correction applied to the data				
composition and uncertainty					
	Ages are quoted at 2s absolute, including				
	dispersion calculated from repeat analyses of				
Uncertainty level and	secondary RMs propagated by quadratic addition.				
propagation	Reproducibility and age uncertainty of reference				
	material and common-Pb composition				
	uncertainty are propagated where appropriate.				

using the Iolite software package (v. 4.8.6) and the Geochronology data reduction scheme (DRS) (Paton et al., 2010; 2011). Apatite MAD-UCSB (ID-TIMS total Pb—U isochron = 466.3 \pm 4.0 Ma and (207 Pb/ 206 Pb)_i = 0.703 ± 0.048 ; recalculated with IsoplotR using data in Apen et al., 2022) served as the primary reference apatite for normalization given its homogeneous U-Pb isotopic composition (Apen et al., 2022). Apatites BRZ-1 (ID-TIMS total Pb-U isochron = 2078 ± 13 Ma and $(^{207}\text{Pb}/^{206}\text{Pb})_i = 1.135 \pm 0.100$; Apen et al., 2022), MRC-1 (ID-TIMS) total Pb—U isochron = 153.3 \pm 0.2 Ma and (207 Pb/ 206 Pb)_i = 0.854 \pm 0.023; recalculated with IsoplotR using data in Apen et al., 2022), and McClure Mountain (ID-TIMS total Pb—U isochron = 525.3 \pm 1.7 Ma and $(^{207}\text{Pb}/^{206}\text{Pb})_i = 0.875 \pm 0.009;$ recalculated with IsoplotR using data in Schoene and Bowring, 2007, and Krestianinov et al., 2021) used as secondary reference apatites to assess accuracy and precision. Repeat analyses of the secondary reference apatites over the course of this study indicate that each ²³⁸U/²⁰⁶Pb and ²⁰⁷Pb/²⁰⁶Pb measurement require an additional uncertainty of 2.5% and 2.2%, respectively, to achieve MSWDs acceptable for single age populations (Wendt and Carl, 1991);

these values were added in quadrature to the internal uncertainty of each U—Pb datum (Horstwood et al., 2016). The final U—Pb ratios and uncertainties (all 2 s) were plotted on Tera-Wasserburg diagrams using IsoplotR, with isochrons calculated using discordia model-1 (Vermeesch, 2018). In samples showing overdispersion, we report an uncertainty augmented by a factor of \(\sqrt{MSWD} \) (Vermeesch, 2018).

The $^{204}\text{Pb}/^{206}\text{Pb}$ ratios and associated uncertainties were calculated in MATLAB using the baseline-subtracted time series data output from Iolite. Cell carrier gas flow rates were tuned to minimize the ²⁰²Hg signal while also enabling sufficiently rapid washout (Table 2). The baselinesubtracted ²⁰²Hg signals for all the apatites were consistent (~4.0 E-7 V), whereas the ²⁰²Hg signals for NIST612 measured in the same session were slightly higher (~6 E-7 V). Following Horstwood et al. (2003), we corrected for the ²⁰⁴Hg isobaric interference on ²⁰⁴Pb using the measured ²⁰²Hg and a ²⁰⁴Hg/²⁰²Hg natural isotopic composition of 0.229230 (Meija et al., 2016). Mass-bias corrections were done using NIST612 silicate glass (Woodhead and Hergt, 2001). Based on several iterations of sensitivity testing, mass-bias factors were found to have a negligible effect on ²⁰⁴Hg-corrections. The ²⁰⁴Hg-corrected ²⁰⁴Pb/²⁰⁶Pb ratios were normalized to the MAD-UCSB primary apatite (204 Pb/ 206 Pb $= 0.005015 \pm 0.000109$; Apen et al., 2022). An additional uncertainty of 2.1% was propagated to each ²⁰⁴Pb/²⁰⁶Pb measurement based on the dispersion in the primary apatite ²⁰⁴Pb/²⁰⁶Pb ratios measured during the analytical session (Horstwood et al., 2003).

Trace-element abundances were calculated in Iolite using the Trace_Element DRS (Woodhead et al., 2007). We utilized ⁴⁴Ca as the internal standard element, assuming stoichiometric abundances of Ca in fluorapatite (39.74 wt%). The NIST 612 silicate glass (Pearce et al., 1997) was used for calibration (preferred values of Jochum et al., 2011). The uncertainty of each element reflects only the internal uncertainty. The complete U—Pb and trace element LASS data set is presented in Supplementary Table 2.

3. Results

3.1. CL images

FCT apatite grains are largely homogeneous, but discrete cores (< 40-µm-diameter) with oscillatory zonation are present in some grains (Fig. 1A). Small (< 20-µm-diameter) quartz and feldspar inclusions are observed in FCT apatite, identified using energy dispersive spectroscopy. MD apatite crystals are unzoned and are generally free of inclusions (Fig. 1B). TEM2 apatites comprise two distinct populations. One population displays mottled, patchy textures of intergrown CL bright and dark domains. The other population is generally homogeneous, though some of these grains have thin (< 2-um-thick) CL-dark rims (Fig. 1C). AS apatite has faint sector-zoning but is overall homogeneous (Fig. 1D).

3.2. U—Pb ID-TIMS geochronology

We applied multiple common-Pb correction schemes to calculate isochrons and ($^{207}\text{Pb}/^{206}\text{Pb}$)_i ratios for each of the apatite samples. The corrections include application of an age-appropriate Stacey and Kramers (1975) model common-Pb composition, unanchored 2-D regressions in $^{238}\text{U}/^{206}\text{Pb}-^{207}\text{Pb}/^{206}\text{Pb}$ space, and unanchored 3-D regressions in $^{238}\text{U}/^{206}\text{Pb}-^{207}\text{Pb}/^{206}\text{Pb}-^{204}\text{Pb}/^{206}\text{Pb}$ space. A summary of calculated isochrons and ($^{207}\text{Pb}/^{206}\text{Pb}$)_i ratios is presented in Table 3.

Nine FCT apatite grains were analyzed. Of these, one analysis is omitted from further discussion due to an exceedingly low radiogenic Pb (Pb*) to common Pb (Pb_c) ratio (Pb*/Pb_c < 0.001). The other eight grains (Pb*/Pb_c > 0.010) have Th/U ratios of 0.5–1.5. The eight aliquots together produce isochrons with MSWDs higher than acceptable for a single age population (Wendt and Carl, 1991), regardless of the applied common-Pb correction method (Table 3). Anchoring these analyses to a Stacey and Kramers (1975) ($^{207}\text{Pb}/^{206}\text{Pb})_i = 0.837$ yields a 22.6 \pm 1.5

Table 3Calculated U—Pb isochrons using different common-Pb corrections.

apatite	method	Stacey and Kramers (1975)		$^{238}\text{U}/^{206}\text{Pb}-^{207}\text{Pb}/^{206}\text{Pb}$ isochron		$^{238}\text{U}/^{206}\text{Pb-}^{207}\text{Pb}/^{206}\text{Pb-}^{204}\text{Pb}/^{206}\text{Pb}$ isochron				
		age (Ma) ¹	$(^{207} Pb/^{206} Pb)_{i}$	MSWD (n)	age (Ma) ¹	$(^{207}\text{Pb}/^{206}\text{Pb})_{i}$	MSWD (n)	age (Ma) ¹	$(^{207}\text{Pb}/^{206}\text{Pb})_{i}$	MSWD (n)
FCT	ID-TIMS	22.6 ± 1.5	0.837	150 (8)	28.6 ± 5.7	0.851 ± 0.001	96 (8)	28.8 ± 3.7	0.851 ± 0.021	320 (8)
	LASS	25.5 ± 7.3	0.837	3.0 (38)	25.1 ± 8.2	0.834 ± 0.018	3.1 (38)	25.5 ± 5.1	0.835 ± 0.020	2.3 (38)
MD	ID-TIMS	98.5 ± 1.1	0.842	2.1 (8)	98.5 ± 1.1	0.840 ± 0.002	2.4 (8)	98.4 ± 0.5	0.839 ± 0.003	9.1 (8)
	LASS	99.9 ± 3.5	0.842	2.1 (40)	99.7 ± 3.7	0.838 ± 0.011	2.1 (40)	97.9 ± 2.5	0.833 ± 0.010	2.0 (40)
TEM2	ID-TIMS	404 ± 18	0.864	3.3 (7)	400 ± 14	0.836 ± 0.014	2.6 (7)	402 ± 7	0.839 ± 0.008	4.5 (7)
	LASS	434 ± 15	0.864	2.4 (40)	431 ± 17	0.855 ± 0.021	2.2 (40)	424 ± 15	0.843 ± 0.028	2.5 (40)
AS	ID-TIMS	1089 ± 11	0.917	110 (8)	1075 ± 18	0.842 ± 0.009	84 (8)	1077 ± 9	0.849 ± 0.046	160 (8)
	LASS	1100 ± 9	0.917	1.5 (40)	1100 ± 8	0.928 ± 0.033	1.4 (40)	1095 ± 13	0.917 ± 0.075	2.6 (40)
BRZ-1	LASS	2045 ± 16	1.010	0.3 (13)	N/A	N/A	N/A	N/A	N/A	N/A
MRC-1	LASS	153 ± 2	0.846	1.7 (13)	N/A	N/A	N/A	N/A	N/A	N/A
McClure	LASS	516 ± 3	0.872	1.2 (40)	518 ± 6	0.878 ± 0.017	1.2 (40)	516 ± 6	0.873 ± 0.020	1.4 (40)

N/A indicates samples do not define an isochron.

¹ Uncertainties are 2 s. In samples with overdispersion, the uncertainty is augmented by a factor of $\sqrt{\text{MSWD}}$ (Vermeesch, 2018).

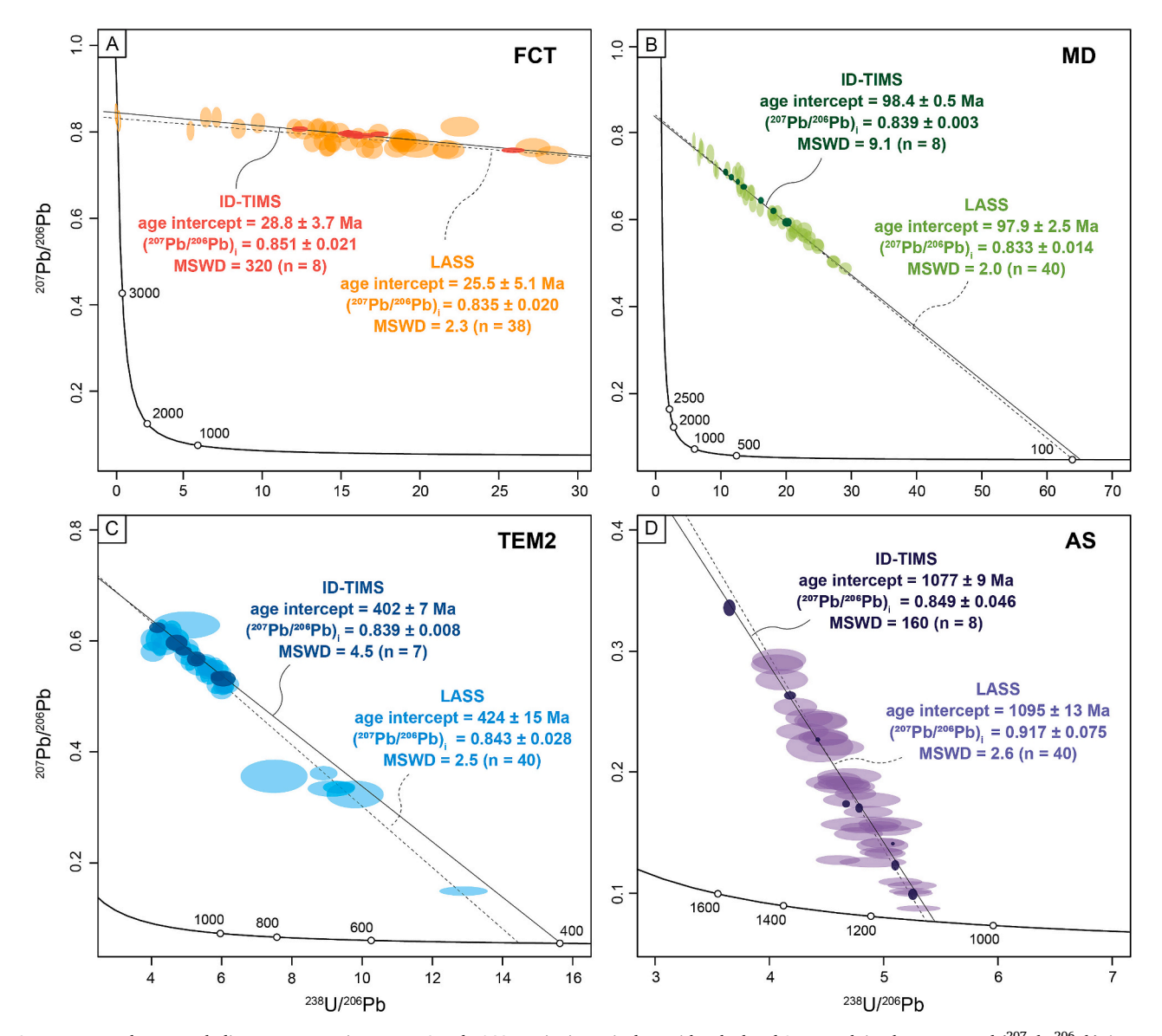


Fig. 2. Tera-Wasserburg U—Pb diagrams comparing ID-TIMS and LASS apatite isotopic data with calculated 3-D U—Pb isochron ages and $(^{207}\text{Pb}/^{206}\text{Pb})_i$ intercepts. Note that all the plotted ID-TIMS data are larger than their actual uncertainties for visualization. A) Fish Canyon apatite plots near the common-Pb endmember and produces isochrons and common-Pb compositions with high uncertainty. B) Mount Dromedary apatite produces well-defined U—Pb isochrons. C) TEMORA 2 apatite analyses show limited Pb*/Pbc ratios. Five LASS data points spread closer to concordia. D) Duluth anorthosite apatite produces well-defined U—Pb isochrons.

Ma isochron (MSWD = 150; n = 8). A 2-D regression produces a 28.6 ± 5.7 Ma isochron with $(^{207}\text{Pb}/^{206}\text{Pb})_i = 0.851 \pm 0.001$ (MSWD = 96; n = 8). A 3-D regression produces a 28.8 ± 3.7 Ma isochron with $(^{207}\text{Pb}/^{206}\text{Pb})_i = 0.851 \pm 0.021$ (MSWD = 320; n = 8).

The eight analyzed MD apatite crystals have Th/U ratios between 2.0 and 2.7 and Pb*/Pb_c ratios between 0.09 and 0.20. The eight analyses produce isochrons with MSWDs higher than accepted for a single age population (Wendt and Carl, 1991). A 2-D regression using a Stacey and Kramers (1975) (207 Pb/ 206 Pb) $_i$ = 0.842 yields a 98.5 \pm 1.1 Ma isochron (MSWD = 2.1; n = 8). A 2-D regression produces 98.5 \pm 1.1 Ma isochron with (207 Pb/ 206 Pb) $_i$ = 0.840 \pm 0.002 (MSWD = 2.4; n = 8). A 3-D regression produces 98.4 \pm 0.5 Ma isochron with (207 Pb/ 206 Pb) $_i$ = 0.839 \pm 0.003 (MSWD = 9.1; n = 8).

Seven TEM2 apatite grains were analyzed using ID-TIMS. These grains have Th/U ratios between 1.7 and 2.3 and Pb*/Pb_c ratios of 0.16–0.23. Use of a Stacey and Kramers (1975) (207 Pb/ 206 Pb)_i = 0.864 as an anchor for a 2-D U—Pb regression yields a 404 \pm 18 Ma isochron (MSWD = 3.3; n = 7). A 2-D regression produces a 400 \pm 14 Ma isochron with (207 Pb/ 206 Pb)_i = 0.836 \pm 0.014 (MSWD = 2.6; n = 7). A 3-D regression produces a 402 \pm 7 Ma isochron with (207 Pb/ 206 Pb)_i = 0.839 \pm 0.008 (MSWD = 4.5; n = 7). All the isochrons for TEM2 have MSWDs greater than expected for a single age population (Wendt and Carl. 1991).

Nine AS apatite crystals were analyzed using ID-TIMS as part of this study. One analysis yields relatively high uncertainty (>1.5% 2σ uncertainty) due to poor UO $_2$ ionization, and as a result is omitted from further consideration. The remaining eight AS apatite analyses have Th/U ratios of 1.9–3.4 and Pb*/Pb $_{c}$ ratios between 0.8 and 14.3. Anchoring the U—Pb regression to a Stacey and Kramers (1975) $\binom{207}{Pb}/\binom{206}{Pb}_{i}=0.917$ yields a 1089 ± 11 Ma isochron (MSWD = 110; n = 8). A 2-D regression produces a 1075 ± 18 Ma isochron with $\binom{207}{Pb}/\binom{206}{Pb}_{i}=0.842\pm0.009$ (MSWD = 84; n = 8). A 3-D regression produces a 1077 ± 9 Ma isochron with $\binom{207}{Pb}/\binom{206}{Pb}_{i}=0.849\pm0.046$ (MSWD = 160; n = 8).

3.3. U-Pb LASS-ICP-MS geochronology

We applied a range of common-Pb corrections to calculate isochrons from each of the samples analyzed by LASS. The isochrons and $(^{207}\text{Pb}/^{206}\text{Pb})_i$ ratios calculated using these different methods for both the newly characterized reference apatites, as well as BRZ-1, MRC-1, and McClure Mountain, are presented in Table 3.

Of the 40 LASS analyses of FCT apatite, two analyses are excluded from the calculations due to incorporation of feldspar inclusions during ablation (e.g., elevated Si and Sr concentrations and low REE concentrations) (open ellipses in Fig. 2A). FCT apatite has variable U and Th (6–40 ppm U and 20–120 ppm Th). Like the ID-TIMS data, isochrons calculated using different common-Pb correction methods all yield MSWDs larger than expected for a single population (Wendt and Carl, 1991). Anchoring these data to a Stacey and Kramers Pb_c composition yields a 25.5 ± 7.3 Ma isochron (MSWD = 3; n = 38). A 2-D regression produces 25.1 ± 8.2 Ma isochron with $(^{207}\text{Pb}/^{206}\text{Pb})_i = 0.834 \pm 0.018$ (MSWD = 3.1; n = 38). A 3-D regression produces a 25.5 ± 5.1 Ma isochron with $(^{207}\text{Pb}/^{206}\text{Pb})_i = 0.835 \pm 0.020$ (MSWD = 2.3; n = 38).

Forty LASS analyses of MD apatite have variable U and Th concentrations (10–60 ppm U and 40–130 ppm Th). The isochrons calculated from the LASS U—Pb data yield MSWDs higher than acceptable for a single population (Wendt and Carl, 1991). Use of a Stacey and Kramers Pb_c composition yields a 99.9 \pm 3.5 Ma isochron (MSWD = 2.1; n=40). A 2-D regression produces a 99.7 \pm 3.7 Ma isochron with ($^{207}\text{Pb}/^{206}\text{Pb})_i$ = 0.838 \pm 0.011 (MSWD = 2.1; n = 40). A 3-D regression produces a 97.9 \pm 2.5 Ma isochron and ($^{207}\text{Pb}/^{206}\text{Pb})_i$ = 0.833 \pm 0.014 (MSWD = 2; n = 40).

Forty LASS analyses of TEM2 apatite yield U concentrations between 2 and 25 ppm and Th concentrations between 4 and 50 ppm. Using a Stacey and Kramers Pb_c composition to anchor to the U—Pb data yields a

434 \pm 15 Ma isochron (MSWD = 2.4; n = 40). A 2-D regression produces a 431 \pm 17 Ma isochron and (207 Pb/ 206 Pb) $_i$ = 0.855 \pm 0.021 (MSWD = 2.2; n = 40). A 3-D regression produces a 424 \pm 15 Ma isochron with (207 Pb/ 206 Pb) $_i$ = 0.843 \pm 0.028 (MSWD = 2.5 n = 40).

Forty analyses of AS apatite contain 2–30 ppm U and 4–95 ppm Th and produce a linear U—Pb array (Fig. 2D). Implementation of a Stacey and Kramers Pb_c composition as an anchor for the U—Pb regression produces a 1100 \pm 9 Ma isochron (MSWD = 1.5; n = 40). A 2-D regression of the same data generates a 1100 \pm 8 Ma isochron with $(^{207}\text{Pb}/^{206}\text{Pb})_i = 0.928 \pm 0.033$ (MSWD = 1.4; n = 40). A 3-D regression of these data produces a 1095 \pm 13 Ma isochron and $(^{207}\text{Pb}/^{206}\text{Pb})_i = 0.917 \pm 0.075$ (MSWD = 2.6; n = 40).

3.4. Trace element geochemistry

The apatite samples analyzed in this study are all LREE enriched and exhibit negative Eu anomalies (Fig. 3). The FCT apatite grains yield average compositions of $(\text{La/Gd})_N = 36.9$ and $\text{Eu/Eu}^* = 0.51$ (where $\text{Eu/Eu}^* = \frac{Eu_N}{\sqrt{Sm_N \times Gd_N}}$; all values normalized to the chondrite values of McDonough and Sun, 1995). The MD apatite crystals have average compositions of $(\text{La/Gd})_N = 22.9$ and $\text{Eu/Eu}^* = 0.25$. The TEM2 apatite grains have average compositions of $(\text{La/Gd})_N = 12.6$ and $\text{Eu/Eu}^* = 0.32$. Finally, the AS apatite crystals yield average compositions of $(\text{La/Gd})_N = 10.2$ and $\text{Eu/Eu}^* = 0.07$.

4. Discussion

4.1. Significance of common-Pb corrections and the new apatite U—Pb dates

Within each sample's LASS and ID-TIMS data set, the implementation of different common-Pb correction schemes does not produce resolvable differences in the calculated isochrons (Table 3). Of the strategies employed, we find that the 3-D isochron method yields dates that are more precise than those obtained using a 2-D regression (anchored or unanchored). The 3-D isochron method additionally incorporates a broader set of Pb—Pb and U—Pb isotopic constraints (i.e., inclusion of $^{204}\text{Pb}/^{206}\text{Pb}$), enabling a more complete evaluation of whether the U—Pb isotopic system was a closed or open system in apatite. The treatment of U—Pb apatite data in this way may further reveal complexities that ultimately reflect key aspects of the geological/thermal histories of interest. For these reasons, we propose that the 3-D isochron be the preferred method for high-resolution apatite U—Pb studies (e.g., Schoene and Bowring, 2006; Chew et al., 2011; Paul et al., 2021).

The 3-D isochron method applied to the new ID-TIMS and LASS data sets yields isochrons with MSWDs larger than acceptable for a single age population (Wendt and Carl, 1991), highlighting complexities in the U—Pb systematics of these samples. The overdispersion in the U—Pb data could be analytical and/or geological in origin. In the ID-TIMS data set, we rule out the former issue based on the reproducibility of high-precision U—Pb ET100 standard measurements made during the same analytical period as the apatite crystals. In the LASS data set, we dismiss an analytical origin for overdispersion based on repeat analyses of other secondary reference apatites (i.e., BRZ-1, MRC-1, and McClure Mountain), which yield isochrons with MSWDs that are consistent with single age populations (Table 3). The propagated $\sim\!2\%$ analytical uncertainty thus adequately accounts for secular variation in LASS analyses (Figs. 2, 4). The large MSWDs associated with FCT, MD, TEM2, and AS apatite therefore most likely reflect geologic variability.

The overdispersion in the U—Pb data sets indicates a protracted crystallization period, partial Pb loss during slow cooling, and/or volumetric mixing of different age domains in the apatites. Experimental diffusion data suggest a nominal thermally-mediated volume diffusion closure temperature of 350–550 $^{\circ}$ C for Pb in apatite, depending on grain

F.E. Apen et al. Chemical Geology 661 (2024) 122191

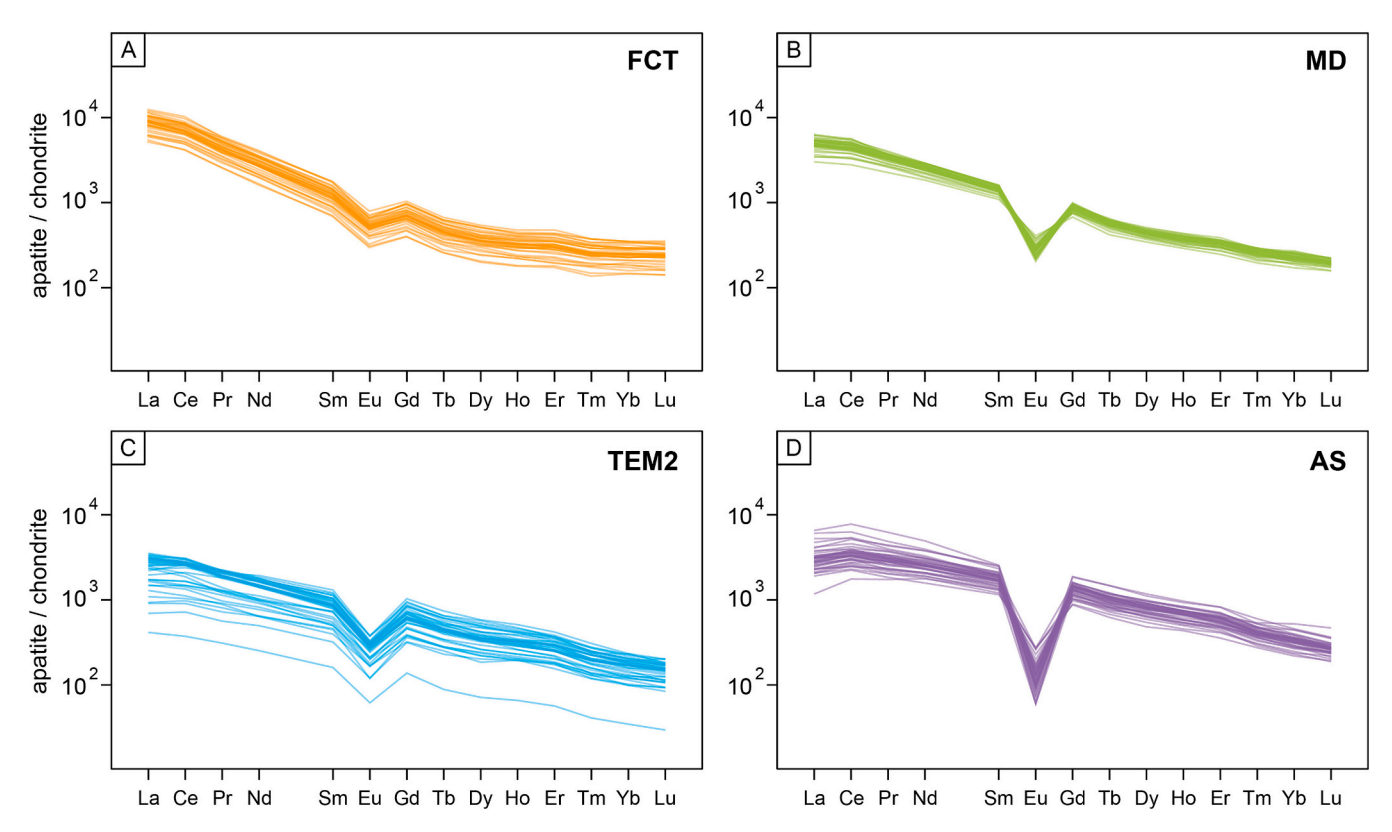


Fig. 3. Chondrite-normalized rare earth element patterns in apatite. In general, all apatite samples are LREE enriched and exhibit negative Eu anomalies. A) Fish Canyon apatite. B) Mount Dromedary apatite. C) TEMORA 2 apatite. D) Duluth anorthosite apatite.

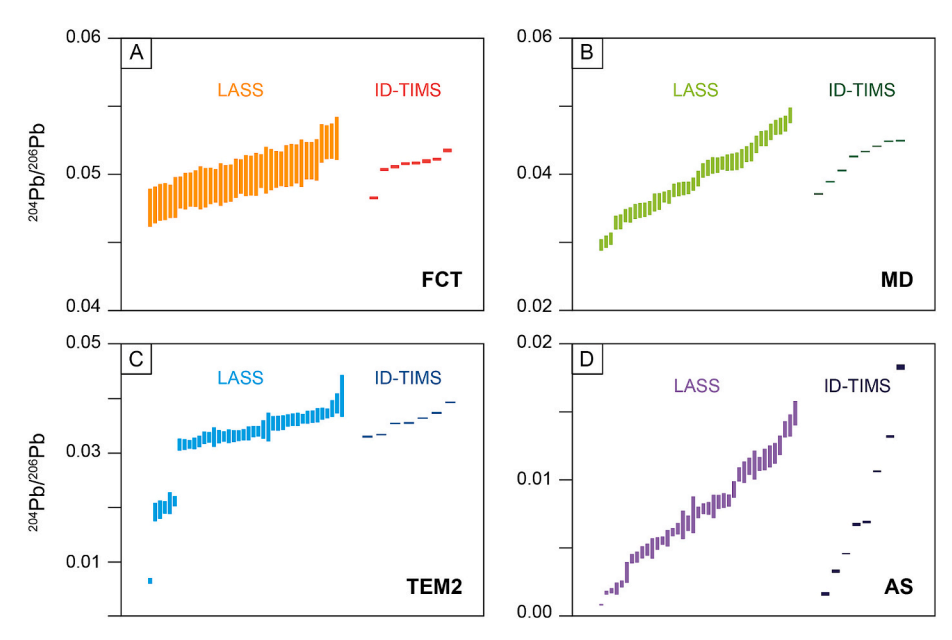


Fig. 4. Comparison of ²⁰⁴Pb/²⁰⁶Pb ratios produced by ID-TIMS and LASS. The LASS ²⁰⁴Pb/²⁰⁶Pb values match the range of ID-TIMS values, confirming the robustness of our ²⁰⁴Pb/²⁰⁶Pb determinations. A) Fish Canyon Tuff apatite. B) Mount Dromedary apatite. C) TEMORA 2 apatite. The five ²⁰⁴Pb/²⁰⁶Pb values below 0.03 are those plotting closer to concordia (Fig. 2C). D) Duluth anorthosite apatite.

size, temperature, and cooling rate (Dodson, 1973; Cherniak et al., 1991). This temperature range is typically below igneous crystallization temperatures relevant to the samples analyzed here. As such, the minor scatter about an isochron may reflect Pb closure of different size grains during cooling (Fig. 1) (e.g., Chamberlain and Bowring, 2001; Schoene and Bowring, 2007; Cochrane et al., 2014; Ibanez-Mejia et al., 2018). The two younger apatite samples analyzed in this study, FCT and MD,

yield dates that are coeval with previously published zircon dates within uncertainty (Fig. 5A, B). The CL images of these samples do not reveal obvious overgrowths or alterations (Fig. 1A, B), suggesting the apatite U—Pb dates reflect instances of rapid cooling in an igneous system (although FCT apatite is likely affected by heterogeneous common-Pb, discussed below). By contrast, the TEM2 and AS apatites yield 3-D isochrons that are younger than their corresponding zircon U—Pb dates

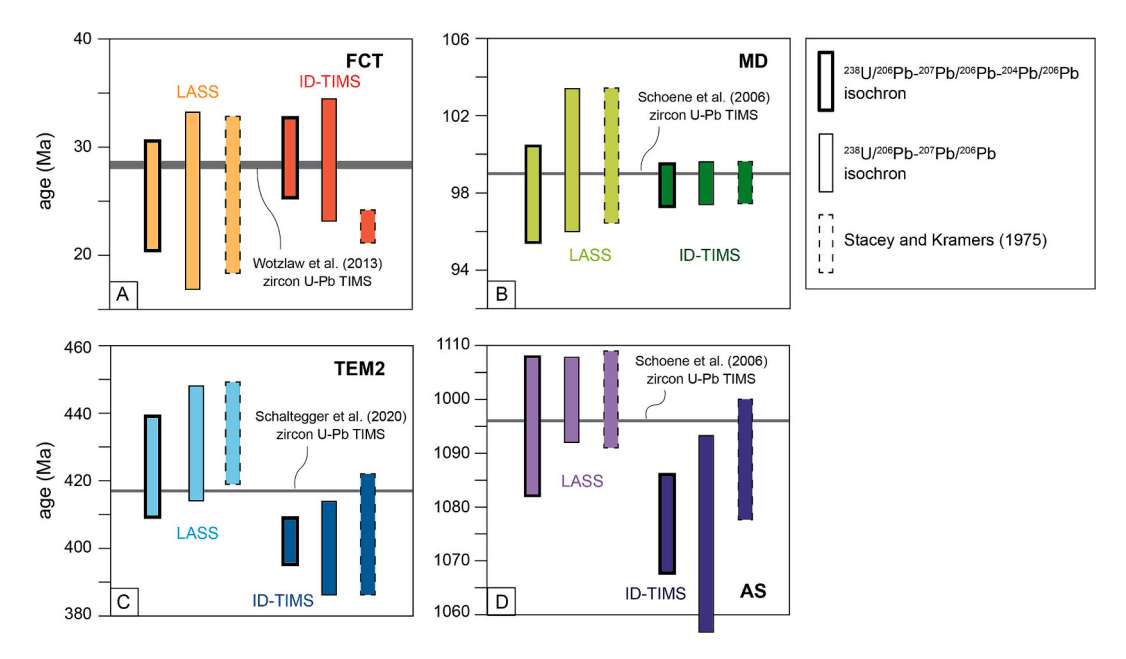


Fig. 5. Comparisons of calculated apatite U—Pb ages with previously published ID-TIMS U—Pb zircon ages. A) Both the LASS and ID-TIMS Fish Canyon apatite ages overlap within uncertainty the zircon dates of Wotzlaw et al. (2013). B) Mount Dromedary apatite ages all overlap the zircon ID-TIMS age reported in Schoene et al. (2006). C) Depending on the common-Pb correction method, TEMORA 2 apatite does (not) overlap the zircon ID-TIMS age reported in Schaltegger et al. (2021). Note that utilizing a Stacey and Kramers model Pb composition produces ages that are older than or equivalent to the zircon age (LASS) or overlaps or post-dates it (ID-TIMS). D) The LASS Duluth anorthosite apatite overlaps the zircon ID-TIMS age reported in Schoene et al. (2006) whereas the ID-TIMS age is equivalent to or post-dates the zircon age depending on common Pb correction method.

beyond 2 s uncertainty, based upon a TEMORA 2 zircon U-Pb CA-ID-TIMS age of 417 Ma (Schaltegger et al., 2021) and a Duluth anorthosite zircon U-Pb CA-ID-TIMS age of 1096 Ma (Schoene et al., 2006). The differences between zircon and apatite ages in these samples are consistent with protracted cooling and/or later resetting by fluidmediated processes. Based on CL images that show overgrowths on otherwise homogeneous grains (Fig. 1C), we infer that TEM2 apatite likely underwent post-crystallization resetting. This is consistent with the mottled textures observed in some TEM2 apatite crystals that are reminiscent of patchy textures observed in metasomatized zircon (e.g., Corfu, 2003). The CL images of Duluth anorthosite apatite show faint sector zonation and no textural evidence for post-igneous crystallization alteration (Fig. 1D). The AS apatite dates may therefore record protracted Pb loss during slow cooling following emplacement of the >10km-thick mafic intrusion (Swanson-Hysell et al., 2021; Härtel et al., 2023). A more detailed assessment of the controls on U-Pb heterogeneity in the apatites would ultimately require additional petrological and microtextural information. Nonetheless, the implementation of 3-D isochrons serves to reveal nuances in the U-Pb data that can help inform geological/thermal histories.

4.2. Limitations of deriving common-Pb compositions from U—Pb apatite analyses

Constraints on common-Pb compositions are necessary for accurate isochron determinations in high Pbc phases, but they can also reveal information about the Pb reservoir from which the phase (re)crystallized (Bellucci et al., 2011; Kirkland et al., 2018; Roberts et al., 2020; Paul et al., 2021). In the case of apatite, U—Pb dates are commonly obtained by regressions with an upper intercept pinned by an assumed bulk evolutionary Pb model composition (e.g., Chew et al., 2014). However, many igneous, metamorphic, and hydrothermal minerals show deviation from these types of evolutionary models, acting as tracers of geologic processes associated with parental sources (e.g., Riciputi and Johnson, 1990; Pettke et al., 2010; Kirkland et al., 2017, 2018; Roberts et al., 2020; Zametzer et al., 2022; Rosera et al., 2023). For instance,

during metamorphism, minerals can (re)crystallize via breakdown of highly radiogenic phases (e.g., Bea and Montero, 1999; Chu et al., 2009; Kirkland et al., 2018) or via reactions with metasomatic fluids (e.g., Glorie et al., 2019; Dusséaux et al., 2022). Therefore, identifying if igneous/metamorphic systems have heterogeneous Pb_c compositions or derive from reservoirs with different evolutionary histories is key to unraveling complex petrogenetic processes.

Regressions of the LASS U—Pb apatite data in this study produce common-Pb compositions that overlap within uncertainty of the nominal Stacey and Kramers (1975) model compositions for rocks of their ages (Fig. 6). However, the higher precision ID-TIMS data for the apatites yield common-Pb compositions that deviate from the model Pb compositions. Given the lower precision associated with modeled Pbc compositions from Stacey and Kramers (1975), utilizing this composition does not necessarily compromise the accuracy of the U—Pb date from either data set (Fig. 5C-D). We therefore suggest that future work be careful before making significant interpretations of Pbc intercepts for petrogenetic studies of U—Pb bearing phases on lower precision techniques, as these data demonstrate that they may not properly delineate different Pb isotopic reservoirs.

Samples with isotopic heterogeneity also present a significant hurdle for age interpretations. The FCT serves as an excellent example of this, as both LASS and ID-TIMS datasets do not generate clear linear relationships in 2-D U—Pb space nor planar relationships in 3-D U—Pb space, as demonstrated by their high MSWDs (Table 3). The CL images of FCT apatite show discrete mantles and cores present in various grains (Fig. 1A). Previous interpretations of the petrology of the FCT have suggested that its minerals record some duration of upper crustal crystallization during pre- and syn-caldera forming phases of the magmatic system, with zircon U—Pb geochronology interpreted to record over 440 kyr of crystallization (e.g., Lipman et al., 1978; Bachmann et al., 2007; Wotzlaw et al., 2013; Morgan et al., 2019). Apatite may have undergone significant Pb diffusion during this interval, as Pb mobility occurs between temperatures of 400-550 °C (Cherniak et al., 1991), well within the range of conditions considered for pre-eruptive magma storage (e.g., Barboni et al., 2016; Rubin et al., 2017). Assuming that the Pb F.E. Apen et al. Chemical Geology 661 (2024) 122191

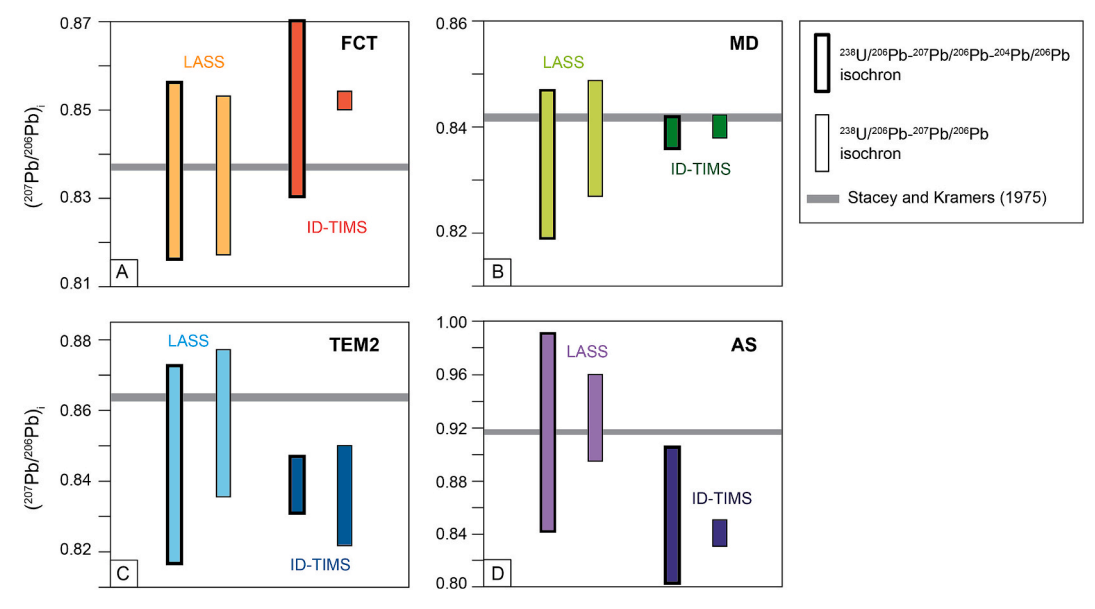


Fig. 6. Comparisons of (207 Pb/206 Pb)₁ from 2-D and 3-D isochron regressions compared to Stacey and Kramers (1975) (horizontal grey bar). A) Common-Pb compositions determined from 2-D and 3-D regressions through Fish Canyon apatite U—Pb data exhibit large uncertainties that overlap with Stacey and Kramers. B) 2-D and 3-D regressions through Mount Dromedary apatite U—Pb data produce common Pb compositions consistent with Stacey and Kramers. C) Regressions through the TEMORA 2 apatite LASS U—Pb data produce common Pb compositions that overlap Stacey and Kramers, but regressions through the ID-TIMS U—Pb data yield compositions that are more radiogenic. D) Regressions through the Duluth apatite LASS U—Pb data produce common Pb compositions that overlap Stacey and Kramers. 2-D and 3-D regressions through the ID-TIMS U—Pb data yield common Pb compositions that are more radiogenic than Stacey and Kramers.

diffusivities reported in Cherniak et al. (1991) are valid for radiogenic Pb, as opposed to lattice bound Pbc, apatite crystals with a 50 µm radius could preserve different age domains at maximum temperatures of 550 °C for 500 kyr; greater temperatures are permissible with shorter durations of heating. As a result, significant Pb diffusion should have occurred in apatite until the period of eruption and subsequent cooling, producing an apatite U—Pb date duration shorter than that of zircon. This dispersion is unlikely to be resolved by the currently available analytical techniques. It is further improbable that the apatite U—Pb dates were reset following eruption, as these rocks do not exhibit significant alteration and were not buried to a significant depth, further supported by the consistent sanidine Ar—Ar geochronology of this unit (e.g., Kuiper et al., 2008; Renne et al., 2010, 2011; Morgan et al., 2014).

Given the <1 Myr pre-eruptive magmatic history of the FCT, it is likely that the U-Pb dispersion present within the FCT apatite data is also driven by heterogeneous Pbc compositions. This interpretation is supported by previously reported initial Pb isotopic compositions of feldspars from the FCT (207Pb/206Pb of feldspars ranging from 0.842 to 0.844, 0.05% 2σ uncertainty), which indicate that individual crystals did not crystallize from a homogeneous magmatic fluid (Lipman et al., 1978; Schmitz and Bowring, 2001). Anchoring the ID-TIMS U-Pb data to an eruption age of 28.2 Ma for the FCT (Kuiper et al., 2008; Rivera et al., 2011) suggests variable (²⁰⁷Pb/²⁰⁶Pb)_i compositions ranging from 0.845 ± 0.001 to 0.856 ± 0.001 . This range is greater and more radiogenic than published feldspar Pb isotopic data (e.g., Lipman et al., 1978; Schmitz and Bowring, 2001). We therefore conclude that the apatite crystallized from a heterogeneous Pb reservoir. If on the other hand apatite and feldspar were in equilibrium prior to eruption of the FCT, the relatively unradiogenic feldspar Pb isotopes would suggest dates younger than determined from 3-D isochrons and from sandine Ar-Ar geochronology (e.g., Kuiper et al., 2008; Renne et al., 2010, 2011; Morgan et al., 2014) and would imply post-eruption disturbances to the U-Pb system in apatite.

The FCT apatite serves as an example of a system with Pb_c compositions that deviates from a Stacey-Kramer model composition but yields new insights into the thermal history associated with the parental magma system of these crystals. We therefore suggest that future U—Pb

geochronology of Pb_c bearing phases consider the possibility that scatter in U—Pb be related to Pb_c heterogeneity and not just age variability. More broadly, our data corroborate previous studies that indicate the use of a Stacey and Kramers Pb evolution model may not always be valid for apatite and other Pb_c bearing phases (Schoene and Bowring, 2006; Paul et al., 2021). Furthermore, given the difference in the Pb_c compositions between the FCT apatite and feldspar crystals, these data also serve as an example of potential pitfalls and inaccuracies that can be raised by using a Pb_c generated by analyzing a different cogenetic low U/Pb mineral phase in a rock of interest. Considering these discrepancies, we again emphasize the advantages of unanchored regressions in generating the most accurate and precise apatite U—Pb dates.

4.3. Viability of reference apatites

The complexities described above notwithstanding; it is useful to establish reference ages for the analyzed apatite samples so that future studies can assess the accuracy of in situ apatite U-Pb data. For reasons already stated, we use the 3-D isochron of the ID-TIMS data as the basis for the reference ages. We assign a reference age of 26.9 \pm 1.7 Ma to FCT apatite but recognize potential heterogeneity in the common-Pb isotopic composition of this sample. The reference age for MD apatite is 98.4 \pm 0.5 Ma (Table 3), in agreement with the 3-D isochron calculated using the LASS data (Fig. 5A, B). The reference age of TEM2 apatite is 402 \pm 7 Ma. Notably, the LASS data includes six radiogenic U-Pb analyses (i.e., those with the highest ²³⁸U/²⁰⁶Pb (Fig. 2C) and lowest ²⁰⁴Pb/²⁰⁶Pb (Fig. 4C)) that are not represented in the ID-TIMS data set. These radiogenic domains were either not sampled by the seven ID-TIMS analyses or, more likely, due to the larger volume of the single TIMS analyses relative to LASS spot analyses, were averaged with the volumetrically dominant less-radiogenic domains. Nevertheless, the 3-D U-Pb isochrons determined for TEM2 using the ID-TIMS and LASS data sets do overlap (Fig. 5C). Lastly, we assign a reference age of 1077 \pm 9 Ma for AS apatite based on the ID-TIMS 3-D isochron, within uncertainty of the 3-D isochron age determined from LASS analyses (Table 3).

Whether the relatively high MSWDs invalidate the samples as viable RMs is a matter of precision of the analytical method employed as the F.E. Apen et al. Chemical Geology 661 (2024) 122191

ability to resolve scatter is a function of individual analysis uncertainty and degree of scatter (e.g., Gaynor et al., 2022). The typical analytical uncertainty of LA-ICP-MS (on the order of 1–2%) may be unable to resolve the variability observed in the ID-TIMS data (typically <1%). With increased precision of in situ methods, future studies should be cognizant of the isotopic heterogeneity in the apatites before employing them as monitors of precision. The ID-TIMS data clearly demonstrates variability in the apatite crystals, such that future high-precision studies should not have the expectation of a single age population in their analyses. The FCT, MD, TEM2, and AS apatites are most useful as secondary RMs for evaluating the efficacy of different common-Pb correction strategies, in particular by providing robust ²⁰⁴Pb data for the implementation of 3-D isochrons (e.g., Horstwood et al., 2003; Gilbert and Glorie, 2020).

5. Conclusions

We report new U—Pb and trace element data for apatites from Fish Canyon Tuff, Mount Dromedary, TEMORA 2, and Duluth Complex anorthosite using ID-TIMS and LASS-ICP-MS and implement multiple common-Pb correction schemes to establish reference ages and common-Pb compositions. The 3-D 238 U/ 206 Pb- 207 Pb/ 206 Pb- 204 Pb/ 206 Pb isochrons determined from ID-TIMS and LASS analyses agree, and we recommend implementation of this method to produce the most accurate and precise U—Pb dates.

Based on the 3-D isochrons of the ID-TIMS data, three of the four analyzed apatites may be suitable as secondary RMs for in situ U-Pb analyses. The reference age of FCT apatite is 28.8 \pm 3.7 Ma with $(^{207}\mbox{Pb}/^{206}\mbox{Pb})_{i} = 0.851 \pm 0.021.$ Given the likely heterogeneity in \mbox{Pb}_{c} in the sample, FCT apatite is unlikely to be a viable U—Pb reference apatite for high-precision U-Pb studies. Mount Dromedary apatite has a reference age of 98.4 \pm 0.5 Ma and $(^{207}\text{Pb}/^{206}\text{Pb})_i = 0.839 \pm 0.003$, consistent with 3-D isochrons determined from LASS analyses. TEMORA 2 apatite, with a reference age of 402 ± 7 Ma and $(^{207}\text{Pb}/^{206}\text{Pb})_i = 0.839$ \pm 0.008, also shows promise as a secondary reference apatite, though its age could be refined with targeted analyses of more radiogenic grains. Apatite from the Duluth Complex anorthosite (from near Forest Center) has a reference age of 1077 \pm 9 Ma with $(^{207}\text{Pb}/^{206}\text{Pb})_i = 0.849 \pm$ 0.046. The common-Pb compositions of TEMORA 2 and Duluth anorthosite apatites deviate from a bulk Pb evolution model, emphasizing that unanchored isochron regressions should be the method of choice for generating the most accurate and precise apatite U—Pb dates. In the case of TEMORA 2 and Duluth anorthosite, the available apatite and zircon U-Pb ID-TIMS ages show resolvable differences, serving as examples wherein using zircon U-Pb dates as reference ages for prospective reference materials from igneous rocks is invalid.

CRediT authorship contribution statement

Francisco E. Apen: Conceptualization, Formal analysis, Investigation, Writing – original draft, Visualization. Sean P. Gaynor: Conceptualization, Formal analysis, Validation, Writing – review & editing. Blair Schoene: Supervision, Writing – review & editing, Validation, Formal analysis. John M. Cottle: Formal analysis, Supervision, Validation, Writing – review & editing.

Declaration of competing interest

The authors declare that they have no known competing financial interests or personal relationships that could have appeared to influence the work reported in this paper.

Data availability

Data included as Supplementary Material

Acknowledgements

This work was supported by a Princeton Presidential postdoctoral fellowship awarded to FA. We thank Paul and Andrea O'Sullivan (GeoSep Services) for providing the apatite separates; Isabel Koran and Travis Steiner-Leach for lending their expertise in the TIMS lab at Princeton; Gareth Seward for acquiring CL images at UCSB; and Andrew Kylander-Clark for technical support with LASS analyses at UCSB. We thank Stijn Glorie and an anonymous reviewer for constructive reviews that helped improve the manuscript, and Marco Fiorentini for editorial handling of the manuscript.

Appendix A. Supplementary data

Supplementary data to this article can be found online at https://doi.org/10.1016/j.chemgeo.2024.122191.

References

- Apen, F.E., Rudnick, R.L., Cottle, J.M., Kylander-Clark, A.R.C., Blondes, M.S., Piccoli, P. M., Seward, G., 2020. Four-dimensional thermal evolution of the East African Orogen: accessory phase petrochronology of crustal profiles through the Tanzanian Craton and Mozambique Belt, northeastern Tanzania. Contrib. Mineral. Petrol. 175, 97. https://doi.org/10.1007/s00410-020-01737-6.
- Apen, F.E., Wall, C.J., Cottle, J.M., Schmitz, M.D., Kylander-Clark, A.R.C., Seward, G.G. E., 2022. Apatites for destruction: Reference apatites from Morocco and Brazil for U-Pb petrochronology and Nd and Sr isotope geochemistry. Chem. Geol. 590, 120689 https://doi.org/10.1016/j.chemgeo.2021.120689.
- Bachmann, O., Bergantz, G.W., 2003. Rejuvenation of the fish Canyon magma body: a window into the evolution of large-volume silicic magma systems. Geol 31, 789. https://doi.org/10.1130/G19764.1.
- Bachmann, O., Oberli, F., Dungan, M.A., Meier, M., Mundil, R., Fischer, H., 2007. 40Ar/39Ar and U-Pb dating of the Fish Canyon magmatic system, San Juan Volcanic field, Colorado: Evidence for an extended crystallization history. Chem. Geol. 236, 134–166. https://doi.org/10.1016/j.chemgeo.2006.09.005.
- Barboni, M., Boehnke, P., Schmitt, A.K., Harrison, T.M., Shane, P., Bouvier, A.-S., Baumgartner, L., 2016. Warm storage for arc magmas. Proc. Natl. Acad. Sci. USA 113, 13959–13964. https://doi.org/10.1073/pnas.1616129113.
- Bea, F., Montero, P., 1999. Behavior of accessory phases and redistribution of Zr, REE, Y, Th, and U during metamorphism and partial melting of metapelites in the lower crust: an example from the Kinzigite Formation of Ivrea-Verbano, NW Italy. Geochim. Cosmochim. Acta 63, 1133–1153. https://doi.org/10.1016/S0016-7037 (98)00292-0
- Bellucci, J.J., McDonough, W.F., Rudnick, R.L., 2011. Thermal history and origin of the Tanzanian Craton from Pb isotope thermochronology of feldspars from lower crustal xenoliths. Earth Planet. Sci. Lett. 301, 493–501. https://doi.org/10.1016/j. epsl.2010.11.031.
- Belousova, E.A., Griffin, W.L., O'Reilly, S.Y., Fisher, N.I., 2002. Apatite as an indicator mineral for mineral exploration: trace-element compositions and their relationship to host rock type. J. Geochem. Explor. 76, 45–69. https://doi.org/10.1016/S0375-6742(02)00204-2.
- Black, L.P., Kamo, S.L., Allen, C.M., Davis, D.W., Aleinikoff, J.N., Valley, J.W., Mundil, R., Campbell, I.H., Korsch, R.J., Williams, I.S., Foudoulis, C., 2004. Improved 206Pb/238U microprobe geochronology by the monitoring of a trace-element-related matrix effect; SHRIMP, ID-TIMS, ELA-ICP-MS and oxygen isotope documentation for a series of zircon standards. Chem. Geol. 205, 115–140. https://doi.org/10.1016/j.chemgeo.2004.01.003.
- Boesen, R.S., Joplin, G.A., 1972. The form of the intrusive complex at mount dromedary, New South Wales. J. Geol. Soc. Aust. 19, 345–349. https://doi.org/10.1080/
- Bruand, E., Fowler, M., Storey, C., Darling, J., 2017. Apatite trace element and isotope applications to petrogenesis and provenance. Am. Mineral. 102, 75–84. https://doi. org/10.2138/am-2017-5744.
- Chamberlain, K.R., Bowring, S.A., 2001. Apatite–feldspar U–Pb thermochronometer: a reliable, mid-range (~450°C), diffusion-controlled system. Chem. Geol. 172, 173–200. https://doi.org/10.1016/S0009-2541(00)00242-4.
- Cherniak, D.J., 2005. Uranium and manganese diffusion in apatite. Chem. Geol. 219, 297–308. https://doi.org/10.1016/j.chemgeo.2005.02.014.
- Cherniak, D.J., Lanford, W.A., Ryerson, F.J., 1991. Lead diffusion in apatite and zircon using ion implantation and Rutherford Backscattering techniques. Geochim. Cosmochim. Acta 55, 1663–1673. https://doi.org/10.1016/0016-7037(91)90137-T.
- Chew, D.M., Sylvester, P.J., Tubrett, M.N., 2011. U–Pb and Th–Pb dating of apatite by LA-ICPMS. Chem. Geol. 280, 200–216. https://doi.org/10.1016/j. chemgeo.2010.11.010.
- Chew, D.M., Petrus, J.A., Kamber, B.S., 2014. U–Pb LA–ICPMS dating using accessory mineral standards with variable common Pb. Chem. Geol. 363, 185–199. https:// doi.org/10.1016/j.chemgeo.2013.11.006.
- Chu, M.-F., Wang, K.-L., Griffin, W.L., Chung, S.-L., O'Reilly, S.Y., Pearson, N.J., Iizuka, Y., 2009. Apatite Composition: Tracing Petrogenetic Processes in

- Transhimalayan Granitoids. J. Petrol. 50, 1829-1855. https://doi.org/10.1093/
- Cochrane, R., Spikings, R.A., Chew, D., Wotzlaw, J.-F., Chiaradia, M., Tyrrell, S., Schaltegger, U., Van Der Lelij, R., 2014. High temperature (>350°C) thermochronology and mechanisms of Pb loss in apatite. Geochim. Cosmochim. Acta 127, 39-56. https://doi.org/10.1016/j.gca.2013.11.028.
- Condon, D.J., Schoene, B., McLean, N.M., Bowring, S.A., Parrish, R.R., 2015. Metrology and traceability of U-Pb isotope dilution geochronology (EARTHTIME Tracer Calibration Part I). Geochim. Cosmochim. Acta 164, 464–480. https://doi.org/ 10.1016/j.gca.2015.05.026.
- Corfu, F., 2003. Atlas of Zircon Textures. Rev. Mineral. Geochem. 53, 469–500. https://
- Corfu, F., Stone, D., 1998. The significance of titanite and apatite U-Pb ages: constraints for the post-magmatic thermal-hydrothermal evolution of a batholithic complex Berens River area, northwestern Superior Province, Canada. Geochim. Cosmochim. Acta 62, 2979-2995. https://doi.org/10.1016/S0016-7037(98)00225
- Dodson, M.H., 1973. Closure temperature in cooling geochronological and petrological systems. Contrib. Mineral. Petrol. 40, 259-274. https://doi.org/10.1007
- Dusséaux, C., Gébelin, A., Boulvais, P., Ruffet, G., Poujol, M., Cogné, N., Branquet, Y., Mottram, C., Barou, F., Mulch, A., 2022. Timing and duration of meteoric water infiltration in the Quiberon detachment zone (Armorican Massif, Variscan belt, France). J. Struct. Geol. 156, 104546 https://doi.org/10.1016/j.
- Eggins, S.M., Grün, R., McCulloch, M.T., Pike, A.W.G., Chappell, J., Kinsley, L., Mortimer, G., Shelley, M., Murray-Wallace, C.V., Spötl, C., Taylor, L., 2005. In situ U-series dating by laser-ablation multi-collector ICPMS: new prospects for Quaternary geochronology. Quaternary Science Reviews 24, 2523-2538. https:// doi.org/10.1016/j.quascirev.2005.07.006
- Eggins, S.M., Kinsley, L.P.J., Shelley, J.M.G., 1998. Deposition and element fractionation processes during atmospheric pressure laser sampling for analysis by ICP-MS. Applied Surface Science 127–129, 278–286. https://doi.org/10.1016/S0169-4332
- Gaweda, A., Szopa, K., Chew, D., O'Sullivan, G.J., Burda, J., Klötzli, U., Golonka, J., 2018. Variscan post-collisional cooling and uplift of the Tatra Mountains crystalline block constrained by integrated zircon, apatite and titanite LA-(MC)-ICP-MS U-Pb dating and rare earth element analyses. Chem. Geol. 484, 191–209. https://doi.org/ 10.1016/j.chemgeo.2018.03.012
- Gaynor, S.P., Ruiz, M., Schaltegger, U., 2022. The importance of high precision in the evaluation of U-Pb zircon age spectra. Chem. Geol. 603, 120913 https://doi.org/ 10.1016/i.chemgeo.2022.120913.
- Gerstenberger, H., Haase, G., 1997. A highly effective emitter substance for mass spectrometric Pb isotope ratio determinations. Chem. Geol. 136, 309-312. https:// doi.org/10.1016/S0009-2541(96)00033-2.
- Gilbert, S.E., Glorie, S., 2020. Removal of Hg interferences for common Pb correction when dating apatite and titanite by LA-ICP-MS/MS. J. Anal. At. Spectrom. 35, 1472–1481. https://doi.org/10.1039/D0JA00224K.
- Glorie, S., Jepson, G., Konopelko, D., Mirkamalov, R., Meeuws, F., Gilbert, S., Gillespie, J., Collins, A.S., Xiao, W., Dewaele, S., De Grave, J., 2019. Thermochronological and geochemical footprints of post-orogenic fluid alteration recorded in apatite: Implications for mineralisation in the Uzbek Tian Shan. Gondwana Res. 71, 1-15. https://doi.org/10.1016/j.gr.2019.01.011.
- Härtel, B., Matthews, W.A., Enkelmann, E., 2023. Duluth complex FC1 Apatite and Zircon: Reference Materials for (U-TH)/he Dating? Geostand. Geoanal. Res. 47, 669-681. https://doi.org/10.1111/ggr.12492.
- Henrichs, I.A., O'Sullivan, G., Chew, D.M., Mark, C., Babechuk, M.G., McKenna, C., Emo, R., 2018. The trace element and U-Pb systematics of metamorphic apatite. Chem. Geol. 483, 218-238. https://doi.org/10.1016/j.chemgeo.2017.12.031
- Henrichs, I.A., Chew, D.M., O'Sullivan, G.J., Mark, C., McKenna, C., Guyett, P., 2019. Trace Element (Mn-Sr-Y-Th-REE) and U-Pb Isotope Systematics of Metapelitic Apatite during Progressive Greenschist- to Amphibolite-Facies Barrovian Metamorphism. Geochem. Geophys. Geosyst. 20, 4103-4129. https://doi.org/ 10.1029/2019GC008359.
- Hiess, J., Condon, D.J., McLean, N., Noble, S.R., 2012. 238 U/ 235 U Systematics in Terrestrial Uranium-Bearing Minerals. Science 335, 1610-1614. https://doi.org/ 10.1126/science.1215507.
- Horstwood, M.S.A., Foster, G.L., Parrish, R.R., Noble, S.R., Nowell, G.M., 2003. Common-Pb corrected in situ U-Pb accessory mineral geochronology by LA-MC-ICP-MS. J. Anal. At. Spectrom. 18, 837-846. https://doi.org/10.1039/B304365G
- Horstwood, M.S.A., Košler, J., Gehrels, G., Jackson, S.E., McLean, N.M., Paton, C., Pearson, N.J., Sircombe, K., Sylvester, P., Vermeesch, P., Bowring, J.F., Condon, D.J., Schoene, B., 2016. Community-Derived Standards for LA - ICP - MS U-(Th-)Pb Geochronology - uncertainty Propagation, Age Interpretation and Data Reporting. Geostand. Geoanal. Res. 40, 311-332. https://doi.org/10.1111/j.1751-908X,2016,00379,x.
- Ibañez-Mejia, M., Tissot, F.L.H., 2019. Extreme Zr stable isotope fractionation during magmatic fractional crystallization. Sci. Adv. 5, eaax8648. https://doi.org/10.1
- Ibanez-Mejia, M., Bloch, E.M., Vervoort, J.D., 2018. Timescales of collisional metamorphism from Sm-Nd, Lu-Hf and U-Pb thermochronology: a case from the Proterozoic Putumayo Orogen of Amazonia. Geochim. Cosmochim. Acta 235, 103-126. https://doi.org/10.1016/j.gca.2018.05.017.
- Jaffey, A.H., Flynn, K.F., Glendenin, L.E., Bentley, W.C., Essling, A.M., 1971. Precision Measurement of Half-lives and specific Activities of U 235 and U 238. Phys. Rev. C 4, 1889–1906. https://doi.org/10.1103/PhysRevC.4.1889.
- Jochum, K.P., Weis, U., Stoll, B., Kuzmin, D., Yang, Q., Raczek, I., Jacob, D.E., Stracke, A., Birbaum, K., Frick, D.A., Günther, D., Enzweiler, J., 2011. Determination

- of Reference Values for NIST SRM 610-617 Glasses following ISO guidelines. Geostand. Geoanal. Res. 35, 397-429. https://doi.org/10.1111/j.1751-908X.2011.00120.x
- Keller, C.B., Schoene, B., Samperton, K.M., 2018. A stochastic sampling approach to zircon eruption age interpretation. Geochem. Persp. Let. 31-35 https:/
- Kirkland, C.L., Hollis, J., Danišík, M., Petersen, J., Evans, N.J., McDonald, B.J., 2017. Apatite and titanite from the Karrat Group, Greenland; implications for charting the thermal evolution of crust from the U-Pb geochronology of common Pb bearing phases. Precambrian Res. 300, 107-120. https://doi.org/10.1016/j.
- Kirkland, C.L., Yakymchuk, C., Szilas, K., Evans, N., Hollis, J., McDonald, B., Gardiner, N. J., 2018. Apatite: a U-Pb thermochronometer or geochronometer? Lithos 318-319, 143-157. https://doi.org/10.1016/j.lithos.2018.08.007.
- Krestianinov, E., Amelin, Y., Neymark, L.A., Aleinikoff, J.N., 2021. U-Pb systematics of uranium-rich apatite from Adirondacks: Inferences about regional geological and geochemical evolution, and evaluation of apatite reference materials for in situ dating. Chem. Geol. 581, 120417 https://doi.org/10.1016/j.chemgeo.2021.120417.
- Krogh, T.E., 1973. A low-contamination method for hydrothermal decomposition of zircon and extraction of U and Pb for isotopic age determinations. Geochim. Cosmochim. Acta 37, 485-494. https://doi.org/10.1016/0016-7037(73)90213-5.
- Krogstad, E.J., Walker, R.J., 1994. High closure temperatures of the U-Pb system in large apatites from the Tin Mountain pegmatite, Black Hills, South Dakota, USA. Geochim. Cosmochim. Acta 58, 3845–3853. https://doi.org/10.1016/0016-7037(94)90367-0.
- Kuiper, K.F., Deino, A., Hilgen, F.J., Krijgsman, W., Renne, P.R., Wijbrans, J.R., 2008. Synchronizing Rock Clocks of Earth history. Science 320, 500-504. https://doi.org/
- Kylander-Clark, A.R.C., Hacker, B.R., Cottle, J.M., 2013. Laser-ablation split-stream ICP petrochronology. Chem. Geol. 345, 99-112. https://doi.org/10.1016/j. chemgeo.2013.02.019.
- Lanphere, M.A., Baadsgaard, H., 2001. Precise K-Ar, 40Ar/39Ar, Rb-Sr and U/Pb mineral ages from the 27.5 Ma Fish Canyon Tuff reference standard. Chem. Geol. 175, 653-671, https://doi.org/10.1016/S0009-2541(00)00291-6.
- Lipman, P.W., Doe, B.R., Hedge, C.E., Steven, T.A., 1978. Petrologic evolution of the San Juan volcanic field, southwestern Colorado: Pb and Sr isotope evidence. Geol. Soc. Am. Bull. 89, 59. https://doi.org/10.1130/0016-7606(1978)89<59:PEOTSJ>2.0.
- Ludwig, K.R., 1998. On the Treatment of Concordant Uranium-Lead Ages. Geochimica et Cosmochimica Acta 62, 665–676, https://doi.org/10.1016/S0016-7037(98) 00059-3.
- Ludwig, K.R., 2012. User's Manual for Isoplot 3.75, A Geochronological Toolkit for Microsoft Excel, No. 5. Berkeley Geochronology Center Special Publication.
- Mattinson, J.M., 2005, Zircon II-Pb chemical abrasion ("CA-TIMS") method: Combined annealing and multi-step partial dissolution analysis for improved precision and accuracy of zircon ages. Chem. Geol. 220, 47-66. https://doi.org/10.1016/j. chemgeo.2005.03.011.
- Mattinson, J.M., 2010. Analysis of the relative decay constants of 235U and 238U by multi-step CA-TIMS measurements of closed-system natural zircon samples. Chem. Geol. 275, 186-198. https://doi.org/10.1016/j.chemgeo.2010.05.007
- McDonough, W.F., Sun, S.-S., 1995. The composition of the Earth. Chem. Geol. 120, 223–253. https://doi.org/10.1016/0009-2541(94)00140-4.
 McDougall, I., Roksandic, Z., 1974. Total fusion 40 Ar/ 39 Ar ages using Hifar reactor.
- J. Geol. Soc. Aust. 21, 81–89. https://doi.org/10.1080/00167617408728836.
- McKanna, A.J., Schoene, B., Szymanowski, D., 2024. Geochronological and geochemical effects of zircon chemical abrasion: insights from single-crystal stepwise dissolution experiments. Geochronology 6, 1-20. https://doi.org/10.5194/gchron-6-1-2024
- McLean, N.M., Condon, D.J., Schoene, B., Bowring, S.A., 2015. Evaluating uncertainties in the calibration of isotopic reference materials and multi-element isotopic tracers (EARTHTIME Tracer Calibration Part II). Geochim. Cosmochim. Acta 164, 481-501. /doi.org/10.1016/j.gca.2015.02.040.
- Meija, J., Coplen, T.B., Berglund, M., Brand, W.A., De Bièvre, P., Gröning, M., Holden, N. E., Irrgeher, J., Loss, R.D., Walczyk, T., Prohaska, T., 2016. Isotopic compositions of the elements 2013 (IUPAC Technical Report). Pure Appl. Chem. 88, 293-306. https://doi.org/10.1515/pac-2015-0503
- Morgan, L.E., Johnstone, S.A., Gilmer, A.K., Cosca, M.A., Thompson, R.A., 2019. A supervolcano and its sidekicks: A 100 ka eruptive chronology of the Fish Canyon Tuff and associated units of the La Garita magmatic system, Colorado, USA. Geology 47, 453-456. https://doi.org/10.1130/G45898.1.
- Morgan, L.E., Mark, D.F., Imlach, J., Barfod, D., Dymock, R., 2014. FCs-EK: a new sampling of the fish Canyon Tuff 40 Ar/ 39 Ar neutron flux monitor. SP 378, 63–67. doi.org/10.1144/SP378.21.
- Odlum, M.L., Levy, D.A., Stockli, D.F., Stockli, L.D., DesOrmeau, J.W., 2022. Deformation and metasomatism recorded by single-grain apatite petrochronology. Geology 50, 697-703. https://doi.org/10.1130/G49809.1
- O'Reilly, S.Y., Griffin, W.L., 2000. Apatite in the mantle: implications for metasomatic processes and high heat production in Phanerozoic mantle. Lithos 53, 217-232. https://doi.org/10.1016/S0024-4937(00)00026-8
- O'Sullivan, G., Chew, D., Kenny, G., Henrichs, I., Mulligan, D., 2020. The trace element composition of apatite and its application to detrital provenance studies. Earth Sci. Rev. 201, 103044 https://doi.org/10.1016/j.earscirev.2019.103044
- Paces, J.B., Miller, J.D., 1993. Precise U-Pb ages of Duluth complex and related mafic intrusions, northeastern Minnesota: Geochronological insights to physical petrogenetic, paleomagnetic, and tectonomagnatic processes associated with the 1.1 Ga Midcontinent Rift System. J. Geophys. Res. 98, 13997–14013. https://doi.org/ 10.1029/93JB01159.

- Paton, C., Hellstrom, J., Paul, B., Woodhead, J., Hergt, J., 2011. Iolite: Freeware for the visualisation and processing of mass spectrometric data. J. Anal. At. Spectrom. 26, 2508. https://doi.org/10.1039/c1ja10172b.
- Paton, C., Woodhead, J.D., Hellstrom, J.C., Hergt, J.M., Greig, A., Maas, R., 2010. Improved laser ablation U-Pb zircon geochronology through robust downhole fractionation correction. Geochem Geophys Geosyst 11, 2009GC002618. https:// doi.org/10.1029/2009GC002618.
- Paul, A.N., Spikings, R.A., Chew, D., Daly, J.S., 2019. The effect of intra-crystal uranium zonation on apatite U-Pb thermochronology: a combined ID-TIMS and LA-MC-ICP-MS study. Geochim. Cosmochim. Acta 251, 15–35. https://doi.org/10.1016/j. gca.2019.02.013.
- Paul, A.N., Spikings, R.A., Gaynor, S.P., 2021. U-Pb ID-TIMS reference ages and initial Pb isotope compositions for Durango and Wilberforce apatites. Chem. Geol. 586, 120604 https://doi.org/10.1016/j.chemgeo.2021.120604.
- Pearce, N.J.G., Perkins, W.T., Westgate, J.A., Gorton, M.P., Jackson, S.E., Neal, C.R., Chenery, S.P., 1997. A Compilation of New and published Major and Trace Element Data for NIST SRM 610 and NIST SRM 612 Glass Reference Materials. Geostand. Geoanal. Res. 21, 115–144. https://doi.org/10.1111/j.1751-908X.1997.tb00538.x.
- Pettke, T., Oberli, F., Heinrich, C.A., 2010. The magma and metal source of giant porphyry-type ore deposits, based on lead isotope microanalysis of individual fluid inclusions. Earth Planet. Sci. Lett. 296, 267–277. https://doi.org/10.1016/j. epsl 2010 05 007
- Prent, A.M., Beinlich, A., Raimondo, T., Kirkland, C.L., Evans, N.J., Putnis, A., 2020. Apatite and monazite: an effective duo to unravel superimposed fluid-flow and deformation events in reactivated shear zones. Lithos 376–377, 105752. https://doi. org/10.1016/j.lithos.2020.105752.
- Renne, P.R., Swisher, C.C., Deino, A.L., Karner, D.B., Owens, T.L., DePaolo, D.J., 1998. Intercalibration of standards, absolute ages and uncertainties in 40Ar/39Ar dating. Chem. Geol. 145, 117–152. https://doi.org/10.1016/S0009-2541(97)00159-9.
- Renne, P.R., Mundil, R., Balco, G., Min, K., Ludwig, K.R., 2010. Joint determination of 40K decay constants and 40Ar*/40K for the fish Canyon sanidine standard, and improved accuracy for 40Ar/39Ar geochronology. Geochim. Cosmochim. Acta 74, 5349–5367. https://doi.org/10.1016/j.gca.2010.06.017.
- Renne, P.R., Balco, G., Ludwig, K.R., Mundil, R., Min, K., 2011. Response to the comment by W.H. Schwarz et al. on "Joint determination of 40K decay constants and 40Ar*/ 40K for the fish Canyon sanidine standard, and improved accuracy for 40Ar/39Ar geochronology" by P.R. Renne et al. (2010). Geochim. Cosmochim. Acta 75, 5097–5100. https://doi.org/10.1016/j.gca.2011.06.021.
- Ribeiro, B.V., Lagoeiro, L., Faleiros, F.M., Hunter, N.J.R., Queiroga, G., Raveggi, M., Cawood, P.A., Finch, M., Campanha, G.A.C., 2020. Strain localization and fluid-assisted deformation in apatite and its influence on trace elements and U–Pb systematics. Earth Planet. Sci. Lett. 545, 116421 https://doi.org/10.1016/j.epsl.2020.116421.
- Riciputi, L.R., Johnson, C.M., 1990. Nd- and Pb-isotope variations in the multicyclic central caldera cluster of the San Juan volcanic field, Colorado, and implications for crustal hybridization. Geol 18, 975. https://doi.org/10.1130/0091-7613(1990) 018-c/0975:NAPIVI-2.3.CO;2.
- Rivera, T.A., Storey, M., Zeeden, C., Hilgen, F.J., Kuiper, K., 2011. A refined astronomically calibrated 40Ar/39Ar age for fish Canyon sanidine. Earth Planet. Sci. Lett. 311, 420–426. https://doi.org/10.1016/j.epsl.2011.09.017.
- Roberts, N.M.W., Drost, K., Horstwood, M.S.A., Condon, D.J., Chew, D., Drake, H., Milodowski, A.E., McLean, N.M., Smye, A.J., Walker, R.J., Haslam, R., Hodson, K., Imber, J., Beaudoin, N., Lee, J.K., 2020. Laser ablation inductively coupled plasma mass spectrometry (LA-ICP-MS) U-Pb carbonate geochronology: strategies, progress, and limitations. Geochronology 2, 33–61. https://doi.org/10.5194/gchron-2-33-2020
- Rosera, J.M., Frazer, R.E., Mills, R.D., Jacob, K., Gaynor, S.P., Coleman, D.S., Farmer, G. L., 2023. Fluorine-rich mafic lower crust in the southern Rocky Mountains: the role of pre-enrichment in generating fluorine-rich silicic magmas and porphyry Mo deposits. Am. Mineral. 108, 1573–1596. https://doi.org/10.2138/am-2022-8503.
- Rubin, A.E., Cooper, K.M., Till, C.B., Kent, A.J.R., Costa, F., Bose, M., Gravley, D., Deering, C., Cole, J., 2017. Rapid cooling and cold storage in a silicic magma reservoir recorded in individual crystals. Science 356, 1154–1156. https://doi.org/ 10.1106/crience.acm9270
- Schaltegger, U., Ovtcharova, M., Gaynor, S.P., Schoene, B., Wotzlaw, J.-F., Davies, J.F.H. L., Farina, F., Greber, N.D., Szymanowski, D., Chelle-Michou, C., 2021. Long-term repeatability and interlaboratory reproducibility of high-precision ID-TIMS U-Pb geochronology. J. Anal. At. Spectrom. 36, 1466–1477. https://doi.org/10.1039/D1JA00116G
- Schmitz, M.D., Bowring, S.A., 2001. U-Pb zircon and titanite systematics of the fish Canyon Tuff: an assessment of high-precision U-Pb geochronology and its application to young volcanic rocks. Geochim. Cosmochim. Acta 65, 2571–2587. https://doi.org/10.1016/S0016-7037(01)00616-0.
- Schmitz, M.D., Bowring, S.A., 2003. Constraints on the thermal evolution of continental lithosphere from U-Pb accessory mineral thermochronometry of lower crustal

- xenoliths, southern Africa. Contrib. Mineral. Petrol. 144, 592–618. https://doi.org/ 10.1007/s00410-002-0419-9.
- Schmitz, M.D., Schoene, B., 2007. Derivation of isotope ratios, errors, and error correlations for U-Pb geochronology using ²⁰⁵ Pb- ²³⁵ U-(²³³ U)-spiked isotope dilution thermal ionization mass spectrometric data: U-PB isotope ratio derivation. Geochem. Geophys. Geosyst. 8, n/a-n/a. https://doi.org/10.1029/2006GC001492.
- Schmitz, M.D., Bowring, S.A., Ireland, T.R., 2003. Evaluation of Duluth complex anorthositic series (AS3) zircon AS a U-Pb geochronological standard: new highprecision isotope dilution thermal ionization mass spectrometry results. Geochim. Cosmochim. Acta 67, 3665–3672. https://doi.org/10.1016/S0016-7037(03)00200-X.
- Schoene, B., Bowring, S.A., 2006. U–Pb systematics of the McClure Mountain syenite: thermochronological constraints on the age of the 40Ar/39Ar standard MMhb. Contrib. Mineral. Petrol. 151, 615–630. https://doi.org/10.1007/s00410-006-0077-4
- Schoene, B., Bowring, S.A., 2007. Determining accurate temperature–time paths from U–Pb thermochronology: An example from the Kaapvaal craton, southern Africa. Geochim. Cosmochim. Acta 71, 165–185. https://doi.org/10.1016/j. gca.2006.08.029.
- Schoene, B., Crowley, J.L., Condon, D.J., Schmitz, M.D., Bowring, S.A., 2006. Reassessing the uranium decay constants for geochronology using ID-TIMS U-Pb data. Geochim. Cosmochim. Acta 70, 426–445. https://doi.org/10.1016/j.gea.2005.09.007.
- Seymour, N.M., Stockli, D.F., Beltrando, M., Smye, A.J., 2016. Tracing the thermal evolution of the Corsican lower crust during Tethyan rifting: thermal evolution of rifting. Tectonics 35, 2439–2466. https://doi.org/10.1002/2016TC004178.
- Sha, L.-K., Chappell, B.W., 1999. Apatite chemical composition, determined by electron microprobe and laser-ablation inductively coupled plasma mass spectrometry, as a probe into granite petrogenesis. Geochim. Cosmochim. Acta 63, 3861–3881. https:// doi.org/10.1016/S0016-7037(99)00210-0.
- Smye, A.J., Marsh, J.H., Vermeesch, P., Garber, J.M., Stockli, D.F., 2018. Applications and limitations of U-Pb thermochronology to middle and lower crustal thermal histories. Chem. Geol. 494, 1–18, https://doi.org/10.1016/j.chemgeo.2018.07.003.
- Spell, T.L., McDougall, I., 2003. Characterization and calibration of 40Ar/39Ar dating standards. Chem. Geol. 198, 189–211. https://doi.org/10.1016/S0009-2541(03) 00005-6
- Stacey, J.S., Kramers, J.D., 1975. Approximation of terrestrial lead isotope evolution by a two-stage model. Earth Planet. Sci. Lett. 26, 207–221. https://doi.org/10.1016/ 0012-821X(75)90088-6.
- Storey, C.D., Jeffries, T.E., Smith, M., 2006. Common lead-corrected laser ablation ICP-MS U-Pb systematics and geochronology of titanite. Chem. Geol. 227, 37–52. https://doi.org/10.1016/j.chemgeo.2005.09.003.
- Swanson-Hysell, N.L., Hoaglund, S.A., Crowley, J.L., Schmitz, M.D., Zhang, Y., Miller, J. D., 2021. Rapid emplacement of massive Duluth complex intrusions within the north American Midcontinent Rift. Geology 49, 185–189. https://doi.org/10.1130/G47873.1.
- Szymanowski, D., Schoene, B., 2020. U-Pb ID-TIMS geochronology using ATONA amplifiers. J. Anal. At. Spectrom. 35, 1207–1216. https://doi.org/10.1039/
- Thomson, S.N., Gehrels, G.E., Ruiz, J., Buchwaldt, R., 2012. Routine low-damage apatite U-Pb dating using laser ablation-multicollector-ICPMS: apatite LA-MC-ICPMS U-PB dating. Geochem. Geophys. Geosyst. 13, n/a-n/a. https://doi.org/10.1029/2011GC003928
- Vermeesch, P., 2018. IsoplotR: a free and open toolbox for geochronology. Geosci. Front. 9, 1479–1493. https://doi.org/10.1016/j.gsf.2018.04.001.
- Wendt, I., Carl, C., 1991. The statistical distribution of the mean squared weighted deviation. Chem. Geol.: Isotop. Geoscie. Sect. 86, 275–285. https://doi.org/ 10.1016/0168-9622(91)90010-T.
- Woodhead, J.D., Hellstrom, J., Hergt, J.M., Greig, A., Maas, R., 2007. Isotopic and elemental imaging of geological materials by laser ablation inductively coupled plasma-mass spectrometry. Geostand. Geoanal. Res. 0 https://doi.org/10.1111/ i.1751-908X_2007_00104_x_071117031212003-2??
- Woodhead, J.D., Hergt, J.M., 2001. Strontium, Neodymium and Lead Isotope Analyses of NIST Glass Certified Reference Materials: SRM 610, 612, 614. Geostandards Newsletter 25, 261–266. https://doi.org/10.1111/ji.1751-908X.2001.tb00601.x.
- Wotzlaw, J.-F., Schaltegger, U., Frick, D.A., Dungan, M.A., Gerdes, A., Günther, D., 2013. Tracking the evolution of large-volume silicic magma reservoirs from assembly to supereruption. Geology 41, 867–870. https://doi.org/10.1130/G34366.1.
- Zametzer, A., Kirkland, C.L., Hartnady, M.I.H., Barham, M., Champion, D.C., Bodorkos, S., Smithies, R.H., Johnson, S.P., 2022. Applications of Pb isotopes in granite K-feldspar and Pb evolution in the Yilgarn Craton. Geochim. Cosmochim. Acta 320, 279–303. https://doi.org/10.1016/j.gca.2021.11.029.
- Zirner, A.L.K., Marks, M.A.W., Wenzel, T., Jacob, D.E., Markl, G., 2015. Rare earth elements in apatite as a monitor of magmatic and metasomatic processes: the Ilímaussaq complex, South Greenland. Lithos 228–229, 12–22. https://doi.org/ 10.1016/j.lithos.2015.04.013.